Journal of Vacuum Science and Technology A

RESEARCH ARTICLE | OCTOBER 11 2016

Combinatorial survey of fluorinated plasma etching in the silicon-oxygen-carbon-nitrogen-hydrogen system

Shailesh Dhungana; Bradley J. Nordell; Anthony N. Caruso; Michelle M. Paquette; William A. Lanford; Kris Scharfenberger; Danya Jacob; Sean W. King

Check for updates

J. Vac. Sci. Technol. A 34, 061302 (2016)
https://doi.org/10.1116/1.4964648
CHORUS

View Online
Export Citation

13 November 2025 14:59:35

Micron Ex. 1032, p. 1
Micron v. YMTC
IPR2025-00117

Combinatorial survey of fluorinated plasma etching in the silicon-oxygen-carbon-nitrogen-hydrogen system

Shailesh Dhungana, Bradley J. Nordell, Anthony N. Caruso, and Michelle M. Paquette[a)]
Department of Physics and Astronomy, University of Missouri-Kansas City, Kansas City, Missouri 64110

William A. Lanford
Department of Physics, University at Albany, 1400 Washington Avenue, Albany, New York 12222

Kris Scharfenberger, Danya Jacob, and Sean W. King[b)]
Logic Technology Development, Intel Corporation, 5200 NE Elam Young Parkway, Hillsboro, Oregon 97124

(Received 11 July 2016; accepted 28 September 2016; published 11 October 2016)

New multipass optical lithography patterning methods needed to print features for future <10 nm technologies will demand an increasingly complex combination of hardmasks, antireflection coatings, spacers, and etch stopping materials with distinct yet complementary properties. Finding the right mix, however, has proven particularly challenging given that the materials most commonly used are drawn from a limited set of Si- and C-based solids comprising Si, C, O, N, and H. To understand and maximize the limits of this composition space, the authors have performed a combinatorial survey of the dry etch characteristics for the Si-C-O-N-H system with the goal of understanding material composition–etch interactions and identifying material subclasses with distinct etch properties. Over 50 thin films sampling Si-C-O-N-H composition space were surveyed using two fluorinated etches commonly utilized for selective patterning of SiO_2 and a-SiN:H dielectrics (CHF_3 and CF_4/O_2, respectively). It was found that the incorporation of oxygen in a-SiN:H allowed for significant tuning of the etch rate of a-SiON:H materials relative to SiO_2. Additionally, increasing hydrogen content and nanoporosity significantly increased the etch rate of the various dielectric materials independent of the Si, C, O, and N content. The influence of carbon depended on whether it was incorporated as terminal organic groups, where it resulted in increased etch rates, or directly within the network of the material, where it resulted in decreased etch rates. Silicon- and carbon-rich materials exhibited very low etch rates in both etches and were found to have the most distinct and potentially complementary etch properties relative to SiO_2 and a-SiN:H. Accordingly, a-C:H, a-Si:H, and a-SiC:H merit further examination as hardmask or spacer materials in future multipass patterning processes. © *2016 American Vacuum Society*.
[http://dx.doi.org/10.1116/1.4964648]

13 November 2025 14:59:35

I. INTRODUCTION

For five decades, transistor area count has doubled roughly every two years in accordance with Moore's Law.[1,2] During this time frame, gains in transistor density have come mostly through Dennard dimensional scaling,[3] which has allowed both a reduction in the transistor areal footprint and tremendous gains in device performance.[4] However, Dennard-style transistor scaling has in the recent decade stalled or come to a halt[5,6] due to numerous physical limitations such as an inability to continue gate dielectric thickness scaling beyond a few atomic layers.[7] Nevertheless, gains in transistor areal density and performance have continued as a result of the implementation of high-*k* gate dielectric materials[8] and novel trigate or fin field effect transistor (FET) architectures.[9] Further, a long bench of new and upcoming Omega-FET, Pi-FET, and nanowire transistor devices exist that offer the potential for transistor scaling down to low single nanometer dimensions.[10,11] Beyond these charge-based devices, an equally vast array of novel devices exist that are based on other non-charge-based computational states that offer the potential for further scaling and reduced energy consumption.[12,13]

Unfortunately, the optical lithography techniques utilized to define the shape and dimensions of a transistor (as well as the associated metal interconnect) have faced serious physical scaling limitations of their own.[14] For an optical projection system, resolution (R) is defined by the Rayleigh criterion, $R = \lambda/\mathrm{NA}$, where λ is the wavelength of the imaging light and NA is the numerical aperture of the projection assembly.[15] For current industry-standard 193 nm deep UV projection systems, the predicted minimum achievable resolution is correspondingly ~80–90 nm.[6,15] To achieve the greater resolution needed to print smaller feature sizes, the semiconductor optical lithography roadmap has for over a decade called for implementation of a shorter wavelength light referred to as extreme UV (EUV).[16,17] However, new EUV light sources have faced significant technical challenges that have delayed the target insertion point for EUV lithography numerous times.[18–20] In order to print feature sizes well below the wavelength of light, computational lithography[21] has been utilized extensively, and more recently, pitch division and double-quadruple multiple patterning techniques have allowed features <20 nm to be

[a)]Electronic mail: paquettem@umkc.edu
[b)]Electronic mail: sean.king@intel.com

Micron Ex. 1032, p. 2
Micron v. YMTC
IPR2025-00117

achieved.[22,23] These latter multipatterning approaches break up the targeted pattern to be printed into reduced symmetry segments and rely on multiple combined lithography and etch transfer passes to achieve the final desired feature. The numerous litho and etch iterations, in turn, require a complex stack of hardmask, antireflection, spacer, and photoresist coatings with stringent optical, physical, and etch selectivity requirements.

Because of the likely continued delays in EUV technology, additional complementary processes have been sought to increase the number of degrees of freedom for <10 nm optical lithographic processes. These have included increased usage of self-aligned patterning techniques,[23] implementation of directed-self-assembled block-*co*-polymer photoresists,[24,25] and selective deposition of materials on preformed patterns.[26] While several proof of concepts have been demonstrated in these areas,[27–29] it is likely that multipatterning techniques will continue to be heavily relied on to bail out the lack of optical lithography scaling for single digit nanometer technologies and beyond. This will in turn further increase the complexity and already stringent etch selectivity requirements for multipatterning approaches and essentially require unique combinations of spacer, hardmask, and etch stopping materials that exhibit near perfect etch selectivity to one another in various plasma etch chemistries. As one example,[23,30] a typical multipattern process may employ up to five or more patterning assist materials that must be etched through with varying degrees of selectivity, not including the target material to which the final pattern is to be transferred. Fortunately, this level of complexity can be reduced by consideration of the four color theorem of map topology.[31]

The four color map theorem states that only four colors are needed for coloring any map such that no two countries with a common border will have the same color.[31] Whereas proof of the four color theorem required the invention of the modern day computer,[32] the theorem may in turn be applied to reducing the complexity of multipatterning processes for next-generation microprocessors. Specifically, a multipatterned wafer may be viewed as a checkerboard array of different materials that are exposed simultaneously during any plasma etch transfer step.[33,34] For pure pattern transfer fidelity to be maintained, only one of the exposed materials may be etched by the plasma chemistry while the others must exhibit near perfect etch resistance. This scenario and the associated requirements are analogous to the four color map theorem, which suggests that only four unique material/etch chemistry combinations are needed to enable even the most complex multipatterning process. Unfortunately, even within this simpler framework, the current combination of largely halogenated etch chemistries and pattern stack materials (predominantly all from the Si-O-C-N-H phase diagram) at best present only two unique "colors."[35,36] The few materials from outside the Si-O-C-N-H system that have been identified as viable third color materials [e.g., TiN (Ref. 37)] present additional challenges related to optical transparency, mechanical stability, and defects.[38,39] Thus, new materials that could be viable third or fourth colors are highly desired to increase the flexibility of designing new material stacks to assist future multipatterning processes.

Toward this end, we have begun a search for new materials and material subclasses that, in combination with typical plasma etch chemistries, will allow the identification of potential third and fourth colors. We report a combinatorial plasma etch survey of over 50 different materials commonly utilized in microelectronic processing that have been treated with two fluorinated etches typically used for the selective patterning of SiO_2 interlayer and SiN:H etch stop (ES) dielectrics, CHF_3 and CF_4/O_2, respectively. In contrast to previous etch selectivity studies that typically only survey a limited number of materials and do not consistently report the specific composition of these materials,[40–46] the study described here enables a direct analysis of the influence of material stoichiometry and mass density on blanket/unpatterned etch rates and thus allows a more thorough survey of the etch rate ranges and selectivities possible within a given composition space. It is acknowledged that this study neglects many different pattern-dependent effects that are also important considerations for plasma etch optimization including: fin/trench sidewall tapering,[47,48] faceting,[49] necking,[49] bowing,[50] microtrenching,[50,51] microloading,[52] and reactive ion etch (RIE) lag[53] resulting from topography driven shadowing[54] and/or differential charging.[55] However, we view this approach as an important first step in beginning to understand the role that material composition may play in influencing these effects. It is anticipated that this screening study will thus allow for a more rational selection of a subset of materials from this study for future pattern-dependent-focused etch–material interaction studies.

In this article, we specifically focus on the Si-C-O-N-H phase space that comprises the majority of materials typically involved in multipattern processing. A wide variance in etch rate with composition is observed and points to both Si-C-O-N stoichiometry and mass density/hydrogen content being significant considerations for tuning etch selectivity and identifying potential third and fourth color dielectrics. In a companion article,[56] we focus on several high-dielectric-constant materials (Al_2O_3, AlN, HfO_2) and up-and-coming low-*k* dielectric materials (a-B:H, a-BC:H, a-BN:H, a-BP) that lie completely outside the Si-C-O-N system and represent additional third and fourth color materials.[39] Beyond advancing current state-of-the-art pitch division/multipatterning processes within the nanoelectronics industry, we believe these combined studies will additionally benefit nanoscale fabrication processes for electromechanical, energy storage/harvesting, photovoltaic, optoelectronic, and other micro/nanoelectronic devices.

II. EXPERIMENT

The materials investigated in this study were all deposited on Si (001) substrates using a variety of chemical vapor deposition (CVD), plasma-enhanced CVD (PECVD), and spin-on deposition techniques, the details of which have been provided elsewhere.[57–62] Table I provides a summary

13 November 2025 14:59:35

Micron Ex. 1032, p. 3
Micron v. YMTC
IPR2025-00117

TABLE I. Summary of properties for the various materials in the Si-C-O-N-H system utilized in this study.

Film type	Deposition	Composition range	Density range (g/cm^3)
C:H, CF_x	PECVD, spin-on	H = 25%–50%, F = 0%–44%	0.7–2.2
Si, Si:H	CVD, PECVD	H = 0%–12%	2.2–2.3
SiO_x:H	CVD, PECVD	x = 1.8–2.2, H = 0%–14%	2.2–2.3
SiN_x:H	CVD, PECVD	x = 0.9–1.5, H = 0%–40%	2.0–2.5
SiC_x:H	PECVD	x = 1–4, H = 30%–55%	1.1–2.5
SiO_xN_y:H	PECVD	O = 0%–26%, N = 0%–37%, H = 0%–20%	2.2–2.5
SiN_xC_y:H	PECVD	N = 4%–18%, C = 20%–30%, H = 0%–50%	1.5–2.5
SiO_xC_y:H	PECVD, spin-on	O = 12%–25%, C = 8%–35%, H = 0%–40%	0.9–2.2

of the various films investigated, including their nominal composition and deposition method. The thickness of the films utilized in this study ranged from as thin as 100 nm to as thick as several microns.

The full elemental composition of all films was determined by combined nuclear reaction analysis (NRA) and Rutherford backscattering (RBS) measurements performed at the University of Albany Dynamitron Accelerator Laboratory. This analysis has been described in detail previously.[63] Briefly, the H content was determined using the ^{15}N nuclear reaction method, and the C, N, and O content was determined using deuteron nuclear reactions. The Si content was determined by 2 MeV ^4He RBS. Given the determined H, C, N, O, and Si composition of the films, parameter-free simulations of the full RBS spectra were performed using the program RUMP.[63] These RUMP simulations were then compared to the data to provide a powerful check on the analysis. As an additional consistency check, the mass density for all of the films was determined using both NRA-RBS and previously described x-ray reflectivity measurements.[59] The two techniques were found to be in agreement to within ± 0.1 g/cm^3.

To allow for a direct comparison of the dry plasma etch characteristics of each thin-film material, the samples were all etched simultaneously in a single plasma etch tool. This was accomplished by cleaving $\sim\frac{1}{2}\times 1$ in. coupons of each material from its respective substrate. These coupons were then loaded onto a handler wafer and etched simultaneously in a 300 mm diameter single wafer Oxford Instruments PlasmaLab μEtch 300 RIE system. Portions of each coupon were protected from the plasma etch using a thin Si beam cleaved from a 300 mm diameter Si (001) wafer and physically placed across each row of coupons (see Fig. 1). After etching, the etch rate of each material was determined by either measuring the thickness difference or step height across the exposed and unexposed portions of the coupon. For the former, the thickness of each portion of the coupons was determined using spectroscopic ellipsometry. For the latter, a surface profilometer was used to measure the step height created between the etched and unetched portions of the sample. The surface profilometer was utilized primarily for samples where the unexposed and exposed portions of the films exhibited low color/thickness contrast that complicated the etch rate measurements using the ellipsometer. In several cases, the exposed portion of the film was completely etched away, thus preventing an accurate measurement of the film etch rate. These results were either excluded from the final analysis or marked as a minimum possible etch rate. In other cases, no transition between the exposed and unexposed portions of the samples could be measured. For these samples, the etch rate was concluded to be zero.

To screen the etch selectivity of the various materials under consideration, the samples were exposed to two different plasma etches typically used for selective SiO_2 and a-SiN:H etching. The first plasma etch was a common CHF_3-based chemistry used for selectively etching SiO_2 and low-dielectric-constant (i.e., low-k) a-SiOC:H interlayer dielectrics (ILD) with a a-SiN:H etch stop (hereafter designated as the "ILD" etch). The second plasma etch was a common CF_4/O_2-based chemistry typically utilized to selectively etch a a-SiN:H ES relative to SiO_2 (hereafter designated as the "ES" etch). A summary of the nominal process conditions used for both capacitively coupled plasma etches is provided in Table II. We note that while other etch chemistries might be more typically utilized in pitch division patterning processes, the details of these recipes are not typically published in the open literature. In this regard, the CF_4/O_2 and CHF_3 etch chemistries were specifically selected due to both their complementary selective etching capabilities and the fact that detailed etch process conditions for these

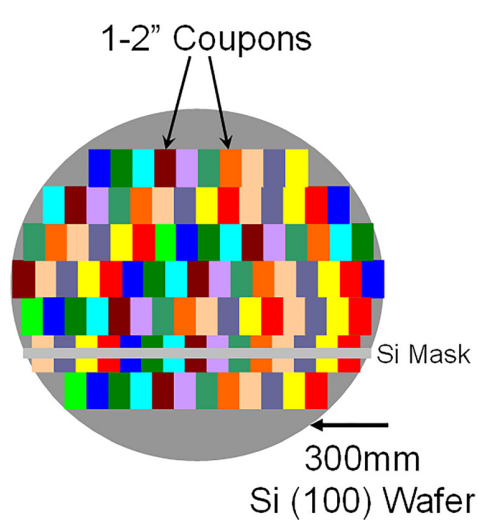

FIG. 1. (Color online) Schematic of wafer carrier and sample geometry for the plasma etch study.

13 November 2025 14:59:35

Micron Ex. 1032, p. 4
Micron v. YMTC
IPR2025-00117

TABLE II. Summary of the RIE process conditions utilized for both the ILD and ES etches.

Process variable	ILD etch	ES etch
CHF_3 (sccm)	38	0
CF_4 (sccm)	0	60
O_2 (sccm)	4	38
Ar (sccm)	38	75
Pressure (Torr)	30	400
RF power (W)	600	280

chemistries are frequently published in the public domain.[39–55]

To account for possible run–run and within chamber variability, each dry etch run was repeated three times and typically included 2–3 replicates of each sample positioned at opposing sites within the chamber. The three runs were performed using different etch times to accommodate the wide variation in thicknesses and etch rates exhibited by the samples in an attempt to avoid having all of the films of a given type be completely etched through or not etched at all. For additional statistical control, six or more CVD SiO_2 samples were also included in each run and randomly distributed within the chamber. The variability/error for the various thickness or step height measurements was generally $\ll 1$ nm and taken to be significantly lower than any sample–sample etch rate variability arising from spatial variations in etch rates within the etch chamber (>1 nm). Additional variability arising from sample–sample composition variability was excluded by utilizing thin film samples with $<3\%$ across wafer composition variability and cleaving replicate samples only from the center of the 300 mm diameter Si (001) wafer. In the results to be presented, we have chosen to plot the results for each individual sample (as opposed to the mean) to more clearly illustrate the number of samples characterized and to highlight any significant sample–sample variability.

In cases where the composition space of a ternary system was sufficiently sampled by the Si-C-O-N-H films investigated in this study, a mixture response surface (RS) analysis was performed using JMP 11.0 statistical analysis software (SAS).[64] The mixture RS analysis specifically used standard least squares and effects screening methods to fit the response (ES or ILD etch rate) to a polynomial that included both linear and two factor elemental composition interaction terms. The resulting coefficient of determination (R^2) from the statistical analysis was used to judge the quality of fit to the polynomial model where R^2 close to 1 indicates an excellent fit and R^2 approaching 0 indicates a poor fit. Ternary response surface contour plots generated within JMP 11.0 were utilized to visually display the fitted and extrapolated RS polynomial model.

III. RESULTS AND DISCUSSION

Because of the large compositional space covered in this study, we begin by first examining the dry etch behavior of the pure elements (i.e., a-C:H, a-Si:H, and a-Si) and a few stoichiometric, low-hydrogen-content compounds present within the Si-C-O-N composition space [i.e., a-SiO_2, a-Si_3N_4:H (20% H) and a-SiC:H (30% H)]. We initially compare the etch rates of the different materials as a function of their mass density. This is both for clarity of presentation and due to an expected intuitive correlation between the etch rate and mass density of a material (i.e., for a fixed number of reactive etch species and fixed composition, etch rate should decrease as the mass/atomic density of the etched material increases). In this regard, etch rate versus mass density comparisons for amorphous thin-film materials are particularly relevant as differences in deposition methods and process conditions can produce materials with significantly different mass/atomic densities.[65] In many cases, the variations in mass density are largely due to differences in the amount of incorporated hydrogen and other hydrogenated terminal groups (e.g., CH_x, NH_x, and OH) which can act as network modifiers and result in more open/lower density network structures with reduced properties.[66–68]

After establishing general trends in dry etch behavior for the elements and stoichiometric compounds, we next probe more complex compositional effects by examining nonstoichiometric materials (SiO_x:H, SiC_x:H, SiN_x:H, SiO_xN_y:H, SiN_xC_y:H, and SiO_xC_y:H) and more closely scrutinizing the influence of hydrogen and carbon content on some of the examined material systems. We place a particular emphasis on comparing the etch behavior of the different material composition classes and conclude by seeking to establish clouds of materials with distinctive etch characteristics that might represent unique etch colors.

A. Pure elements and compounds

Figure 2 summarizes the measured etch rates as a function of mass density for the elemental and stoichiometric compound films exposed to the ES (CF_4/O_2) and ILD (CHF_3) etches. As a reminder, each data point represents the result from a single sample in order to more clearly illustrate the number of samples characterized and highlight any sample–sample variability.

For the ES etched samples, etch rates ranging from <1 Å/s to as high as 24 Å/s were observed. For the a-C:H samples, which were sampled across a range of mass densities from 0.7 to 2.2 g/cm^3, etch rates were found to scale as a function of density. For the highest density a-C:H film (2.2 g/cm^3), a low etch rate of ~ 1 Å/s was observed, similar to the values for the a-Si, a-Si:H, and SiO_2 films with comparable mass densities. As the mass density of the a-C:H films decreased, the ES etch rate increased substantially up to a value of ≥ 20 Å/s for the film with a mass density of 0.7 g/cm^3 (note that this value is a minimum value due to the film being completely etched through). Thus, the a-C:H results clearly illustrate the intuitive correspondence between increasing etch rate and decreasing mass/atomic density. For the a-C:H films examined here, the decrease in mass density is a direct result of hydrogen content steadily increasing from 27% for the highest density film to 53% for the lowest density film. The increasing etch rate with

13 November 2025 14:59:35

Micron Ex. 1032, p. 5
Micron v. YMTC
IPR2025-00117

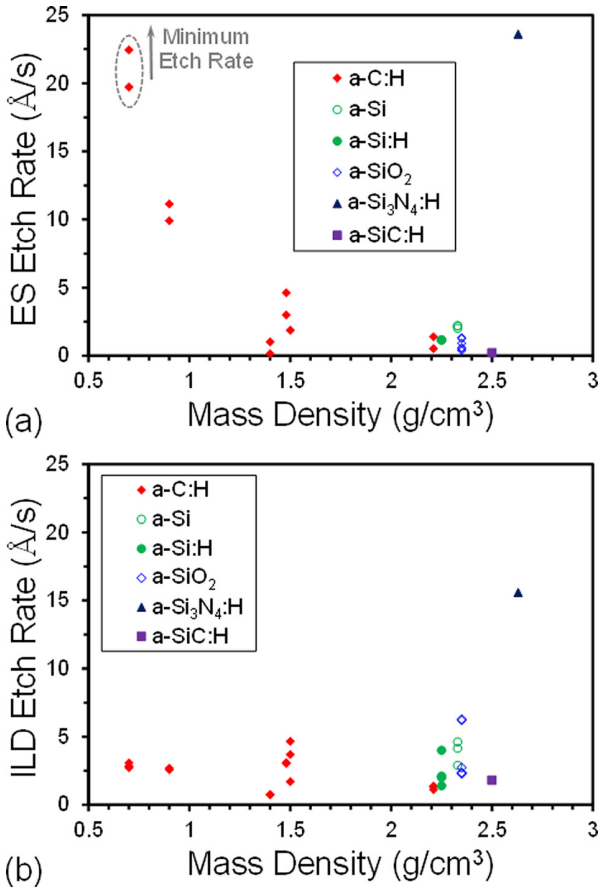

FIG. 2. (Color online) (a) ES (CF_4/O_2) and (b) ILD (CHF_3) etch rates as a function of mass density for a-C:H, a-Si, a-Si:H, a-SiO_2, a-Si_3N_4:H, and a-SiC:H thin films.

hydrogen content can be further rationalized based on the development of interconnected nanoporosity (~25%)[69] in the lowest density a-C:H film that allowed the plasma-activated etch species to penetrate further into the surface of the a-C:H dielectric.[70,71] A similar trend would be expected for a-Si:H, but unfortunately, a-Si:H films with a similarly wide range of hydrogen content could not be obtained for this study.

For all of the Si- and C-based materials in Fig. 2(a), the ES etch rates decreased as a function of material density, with the exception of Si_3N_4:H, which simultaneously exhibits the highest etch rate (24 Å/s) and highest mass density (2.65 g/cm^3). Although perhaps counterintuitive, this result is consistent with the ES etch chemistry being specifically optimized for materials of SiN_x:H composition, and illustrates the additional role of chemical composition/bonding in determining etch rates. Such compositional effects will be further illustrated in more detailed examinations of the ES and ILD etch rates of a-SiO_x:H, a-SiN_x:H, and a-SiC_x:H (vide infra).

For the ILD (CHF_3) etched samples, all of the films exhibited slightly higher but comparable etch rates, with the exception of the PECVD a-Si_3N_4:H film, which—interestingly—again exhibited an etch rate approximately three times as high (~15 Å/s) as that of the CVD SiO_2 film (~5 Å/s) [see Fig. 2(b)]. As we will show later, this difference becomes less apparent for the nonstoichiometric PECVD equivalents of these films (i.e., a-SiN_x:H and a-SiO_x:H). In addition, unlike in the case of the ES etch, the a-C:H films do not exhibit a significant difference in etch rate as a function of mass density for the ILD etch. This can be attributed to the CHF_3 etch being a polymerizing chemistry[35] that, during etching, codeposits surface CF_x that prevents greater subsurface penetration of the plasma-activated etch species.[70,71] In this regard, we note for additional insight that measurements on PECVD CF_x films included with the above samples (but not included in Fig. 2) did show a high etch rate of ~30 Å/s in the CF_4/O_2 ES etch and a substantially lower etch rate of 6 Å/s in the CHF_3 ILD etch. This confirms the partial etch resistance of any surface CF_x residues potentially produced in the CHF_3 chemistry.

B. Nonstoichiometric compounds

We next examine the etch characteristics of several off-stoichiometric materials in the Si-O-C-N-H system. For the ternary and quaternary systems investigated, we initially look at how the etch properties vary in response to a change in concentration for a single element. However, due to limitations associated with the deposition processes, it was difficult in all cases to generate a sample set where the concentration of one element was systematically varied in relation to the concentration of the others. This is particularly true in the case of the plasma-deposited hydrogenated materials where variations in oxygen, nitrogen, and carbon content can cause wide fluctuations in hydrogen content. This point was partly addressed by performing a RS analysis where, for many of the ternary systems investigated, a sufficiently large sampling of the composition space allowed for this. While several RS analysis examples of dry plasma etching have been previously reported in the literature,[72–74] the results presented here differ in that the composition of the material being etched serves as the input variable whereas in prior studies the composition of the plasma etch chemistry and other plasma etch process variables were utilized as inputs.

1. a-SiO_x:H

We begin with the a-SiO_x:H system, for which Fig. 3(a) presents a plot of the ES and ILD etch rates as a function of hydrogen content. As indicated in Table I, a relatively small compositional space of $x = 1.8$–2.2 and H = 0%–14% was explored due to a limited ability to obtain a-SiO_x:H samples with a larger degree of nonstoichiometry. Nevertheless, a slight increase in a-SiO_x:H etch rate for the highest hydrogen content films was observed for both etches. This is consistent with the results for a-C:H for which the ES etch rate was also found to increase with increasing hydrogen content.

As shown in Fig. 3(b), a similar slight increase in a-SiO_x:H ES and ILD etch rates was observed for the samples with the highest x value—that is, the highest oxygen content. This can be attributed to the increased oxygen content being directly correlated to an increased concentration of OH groups.[75] Several previous investigations of the wet etch behavior of a-SiO_2 in hydrogen fluoride (HF) based

13 November 2025 14:59:35

Micron Ex. 1032, p. 6
Micron v. YMTC
IPR2025-00117

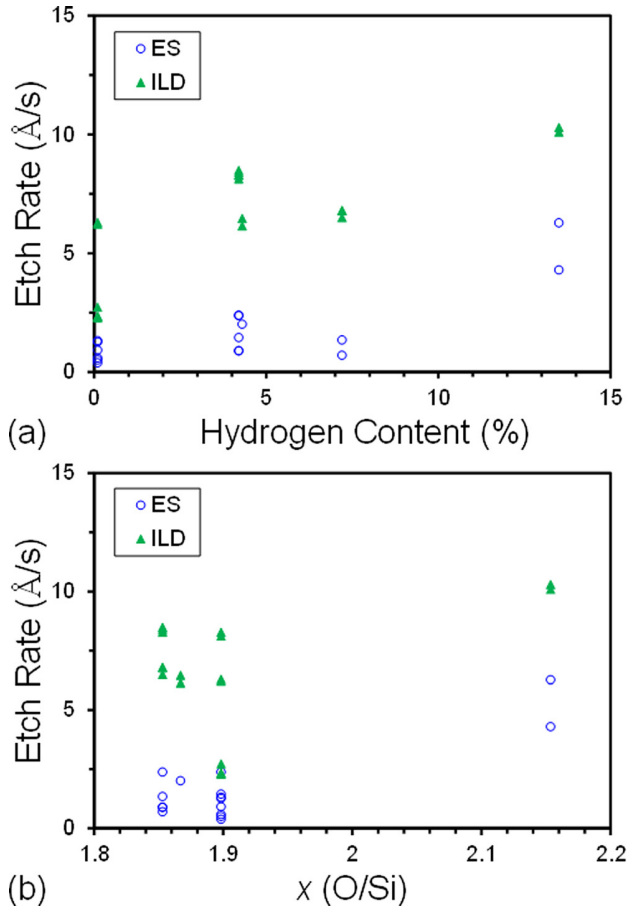

FIG. 3. (Color online) ES and ILD etch rates for a-SiO_x:H thin films as a function of (a) hydrogen content (%) and (b) x (O/Si).

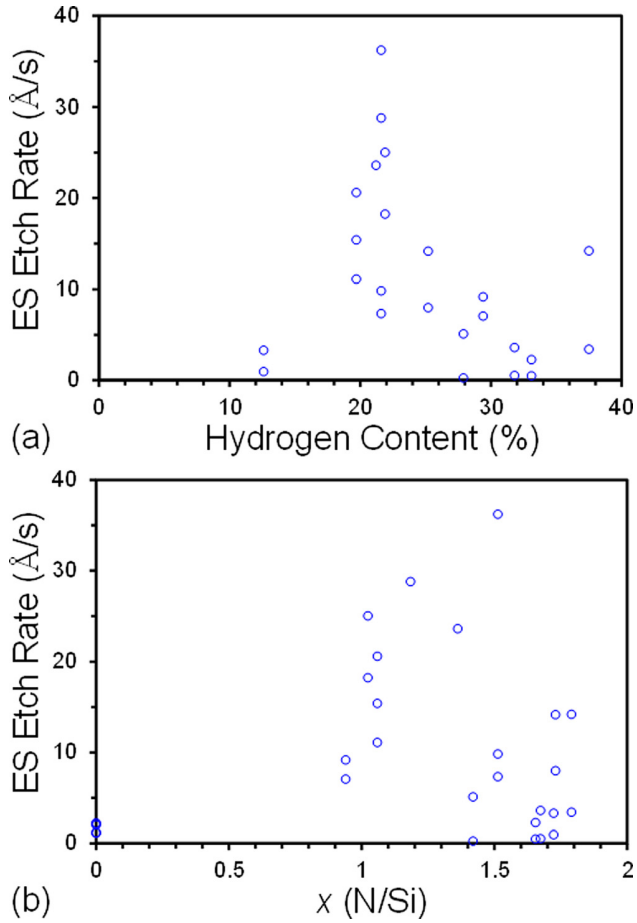

FIG. 4. (Color online) a-SiN_x:H ES etch rates as a function of (a) H content (%) and (b) x (N/Si).

solutions have shown a strong relationship between hydrogen content and HF etch rates.[75,76] However, studies of dry plasma etching of SiO_2 have shown a much weaker effect on hydrogen content.[76]

Since a fairly limited range of x and hydrogen content were investigated in this study, it is possible that a more prominent response between etch rate and composition may exist within the a-SiO_x:H system. However, based on the relatively small differences in etch rate observed in Fig. 2 for a-Si:H and a-SiO_2, one would expect only a rather weak response between x (O/Si) and etch rate. The density trend observed for a-C:H in Fig. 2 does suggest that hydrogen content may have a strong influence on a-SiO_x:H etch rate, but to more clearly observe such an effect would require additional higher hydrogen content samples beyond those available to this study. Due to the limited sampling of the Si-O-H composition space, a more detailed ternary response surface analysis for this system was not attempted.

2. a-SiN_x:H

Figures 4 and 5 present the ES and ILD etch rates, respectively, for a-SiN_x:H as a function of both hydrogen content and N/Si ratio, x. For the ES etch, the a-SiN_x:H etch rate was found in many cases to depend on the etch time, with longer etch times generally leading to higher etch rates (up to 2× in some cases). This is attributed to the formation of a native oxide (SiO_2) surface layer on the a-SiN_x:H films. As shown in Sec. III B 1, SiO_2 exhibits a relatively low ES etch rate and therefore the presence of a thin SiO_x surface layer could be expected to initially impede or delay etching of the underlying a-SiN_x:H film. Similar delayed etch effects have also been reported for plasma etching of silicon and other nitride materials.[77–79] For short etch times, this effect would thus make the measured etch rate appear lower. While this effect increased the variability in the observed a-SiN_x:H ES etch rates, it did not influence the general trends to be discussed.

Focusing on Fig. 4(a), we observe a general decrease in a-SiN_x:H ES etch rate with increasing hydrogen content. This behavior runs counter to the previously observed increasing hydrogen content/increasing etch rate correlation shown in Fig. 2. We also note that the lowest hydrogen content a-SiN_x:H film in Fig. 4(a) actually exhibits a very low ES etch rate in contrast to the observed broader trend. Both of these contradicting observations can be partially understood by examining the ES etch rate dependence on N/Si ratio (x) shown in Fig. 4(b). In this case, a gradual increase in ES etch rate is observed as the N/Si ratio increases from <1 to roughly 1.3–1.4, before it again decreases to low values (note data points for a-Si:H have also been included to allow the full dependence on N/Si ratio to be assessed).

13 November 2025 14:59:35

Micron Ex. 1032, p. 7
Micron v. YMTC
IPR2025-00117

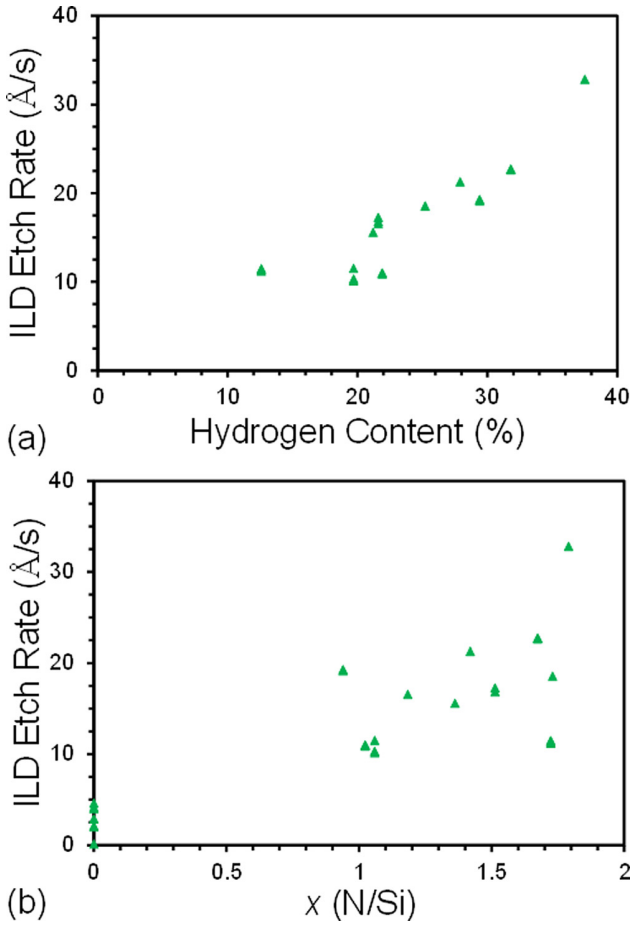

FIG. 5. (Color online) a-SiN_x:H ILD etch rates as a function of (a) H content (%) and (b) x (N/Si).

Thus, the observed maximum in ES etch rate occurs at approximately the same x value as for stoichiometric Si_3N_4 (1.33). This suggests that Si–N bonds are perhaps preferentially attacked/etched by the CF_4/O_2 chemistry relative to the Si–Si, Si–H, and N–H bonds present in higher concentrations in the nonstoichiometric a-SiN_x:H films. In this regard, we note that preferential CF_4/O_2 etching of Si_3N_4 over Si and a-Si:H has been previously reported in the literature.[40,77,80] Thus, the outlier behavior of the lowest hydrogen content a-SiN_x:H film in Fig. 4(a) can be partly attributed to the high N/Si ratio (1.7) exhibited by this film relative to the others. The competing behavior between %H and N/Si on a-SiN_x:H ES etch rate will be more clearly discussed in the response surface analysis described later.

For the CHF_3 ILD etch, the a-SiN_x:H etch rates are slightly higher on average than those observed for the CF_4/O_2 ES etch. This could be due to the higher CHF_3 SiO_2 etch rate and the ability for this etch to more easily break through any SiO_x surface layer present on the a-SiN_x:H films. Interestingly, the ILD etch rate for a-SiN_x:H also shows a strong dependence on hydrogen content, opposite to that found in the case of the ES etch but consistent with the intuitive density/etch rate correspondence, where it increases from ~10 Å/s for 10%–20% H to >30 Å/s for 38% H (see Fig. 5). A similar increase in ILD etch rate with increasing N/Si ratio is also observed, which is rendered even more apparent when including the ILD etch results for a-Si and a-Si:H [see Fig. 5(b)]. This may indicate a weaker selectivity to Si–N bonding for the CHF_3 relative to the CF_4/O_2 chemistry or suggest a stronger dependence on H or Si content for the ILD etch rate.

The strong a-SiN_x:H ILD etch rate dependence on hydrogen content is particularly interesting, given the lack of such an observed dependence for the ILD etch rate of all the other materials discussed so far. As mentioned previously, the lack of a hydrogen content/density trend for the CHF_3 ILD etch in a-C:H and other materials has been attributed to the propensity of this etch to form a comparatively thick CF_x surface layer. In fact, studies by Kuo and others have attributed the selective CHF_3 etching of SiO_2 relative to a-SiN_x:H to the enhanced growth of a CF_x surface layer on a-SiN_x:H.[40,44,45] In this regard, we do note that the a-SiN_x:H film in the Kuo study had a N/Si ratio of 1.6 and hydrogen concentration of 15%, similar to the lowest hydrogen content a-SiN_x:H film examined in this study that also exhibited a relatively low CHF_3 ILD etch rate. Thus, these observations suggest that the CF_x surface layer thickness formed during CHF_3 etching of a-SiN_x:H and other materials is likely dependent on stoichiometry (N/Si), concentration of hydrogen, and/or the presence of specific chemical bonds in the etched film (i.e., C–C, Si–Si, Si–N, Si–C, Si–H, N–H, or C–H).

The contrasting ES and ILD etch behavior may be attributed to differences in the propensity of the two chemistries to etch through a native oxide layer, codeposit CF_x during etching, and the stability of these and other fluoride species on the a-SiN_x:H surfaces. The contrasting dependencies on N/Si and hydrogen content, in particular, suggest variances in sensitivity to different elements or chemical bonds in a-SiN_x:H for the two different etches. Disentangling such effects in a ternary system like a-SiN_x:H can be difficult using simple x–y plots. However, as we will show later, some of these effects can be more clearly analyzed and visualized via a ternary response surface analysis.

To the authors' knowledge, relatively few investigations correlating dry plasma etch rates to variations in a-SiN_x:H properties have been previously reported. However, one detailed investigation worth noting was reported by Hahn *et al.* where the dry etch rates of inductively coupled plasma (ICP) deposited a-SiN_x:H were investigated primarily as a function of film stress and SF_6/Ar ICP etch process conditions.[81] When etch conditions with a strong chemical component were utilized, the authors observed that the measured etch rates increased substantially when the intrinsic film stress increased above 500 MPa. When more physical etch conditions were utilized, the authors observed no apparent dependence of etch rate on film stress. While Hahn *et al.* report only that the refractive index (RI) of the a-SiN_x:H films was ~2.0 and do not report the exact elemental composition, the authors' experience with the a-SiN_x:H films in this study suggests that films with higher compressive stress tend to be closer to the stoichiometric value of $x = 1.33$. In this regard, the increase in SF_6/Ar etch rate with a-SiN_x:H film

13 November 2025 14:59:35

Micron Ex. 1032, p. 8
Micron v. YMTC
IPR2025-00117

stress observed by Hahn is consistent with the maximum in CF_4/O_2 etch rate observed at $x \approx 1.3$ in this study.

To more clearly visualize how both the a-SiN_x:H ES and ILD etch rates vary with composition, a statistical RS analysis was performed. To improve the a-SiN_x:H composition space covered in the analysis, the previously presented results for PECVD a-Si:H and CVD a-Si were also included. The resulting ES and ILD etch rate ternary contour plots predicted from the RS model are depicted in Fig. 6. The filled circular points present in each ternary plot represent the compositions for the individual films utilized in the RS modeling. Each side of the triangle represents the axis for one of the three elemental components of the system (i.e., % Si, N, and H in this case) with the three corners signifying a composition of 100% for each element. The illustrated data points are plotted such that each elemental concentration decreases in proportion to the distance from the corner of the triangle representing that element. The color shading illustrates the ES and ILD etch rates predicted by the RS model as a function of composition.

As evident in Fig. 6, only a portion of the full Si-N-H ternary diagram was sampled in this study. However, a significant portion of this diagram is either experimentally or theoretically known as non film or solid forming. These regions are signified in Fig. 6 by the additional open circle data points which represent compositions where either topological constraint theory predicts networked solid films are not possible,[82,83] or solid films are known not to form (e.g., N_2, NH_3, and H_2 are all gases at room temperature). The latter is signified by the open the circles along the N–H axis at 100% N, 25% N–75% H, and 100% H. The former is represented by the triangle of data points in the right corner of the ternary diagram that is defined by the average bond coordination of the constituent elements and topological bond constraint rules.[82,83] The entire space within the perimeter of this triangle defines compositions where networked films are unlikely.

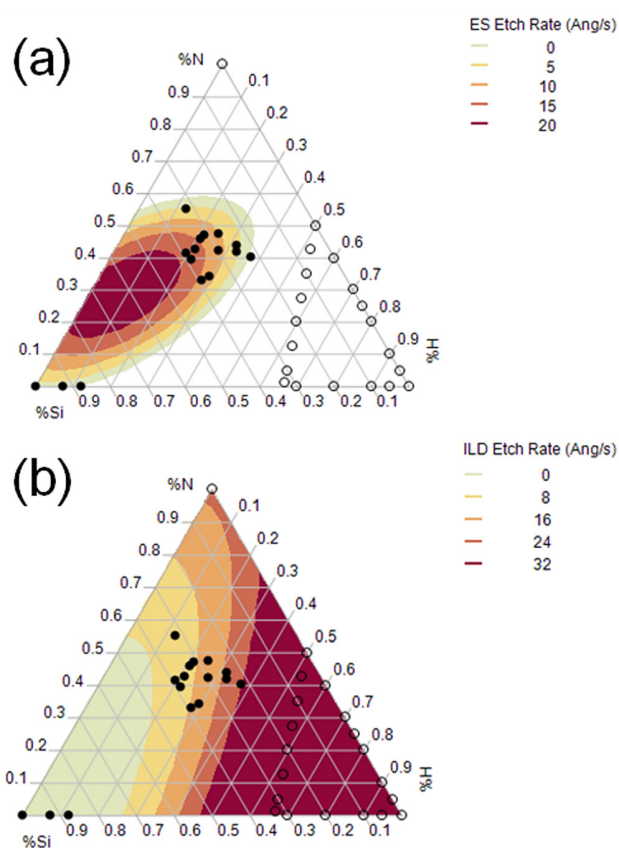

FIG. 6. (Color online) (a) ES and (b) ILD etch rates for a-SiN_x:H as a function of silicon, nitrogen, and hydrogen content (%). Filled circles represent experimental data points and open circles non-film-forming compositions.

For the RS analysis of the a-SiN_x:H ES etch rate, an R^2 value of 0.5 was obtained, indicating that the RS model fitted only 50% of the observed variability in etch rate. Some of the nonfitted variability could be attributed to the clustering of the experimental data points in the center and at the Si corner of the Si-N-H diagram. However, the a-SiN_x:H ES etch rate RS contour profile illustrated in Fig. 6(a) clearly captures the behavior observed in Fig. 4(a) where ES etch rate generally decreases with increasing hydrogen content, and is observed to increase and then decrease with increasing N/Si ratio. This is consistent with the RS model where %Si–%N and %N–%H interactions were found to have higher strength of correlations relative to just %H. Importantly, Fig. 6(a) captures the fact that the low hydrogen content/low ES etch rate outlier in Fig. 4(a) is due to the higher N/Si ratio of this film relative to the other a-SiN_x:H films investigated. This is also consistent with prior studies that have found plasma-deposited nonstoichiometric hydrogenated silicon nitride to have higher CF_4/O_2 etch rates relative to silicon and low hydrogen stoichiometric silicon nitride deposited by chemical vapor deposition.[84]

The maximal ES a-SiN_x:H etch rate predicted by the RS model actually occurs at roughly 60% Si, 30% N, and 10% H. Unfortunately, the predicted maximum falls outside the experimentally sampled portion of the Si-N-H ternary diagram. It is unclear whether such a maximum truly exists or is simply an artifact of the reduced model fit and/or the nonuniform sampling of composition space. Any attempts to extrapolate the results of the a-SiN_x:H ES RS model outside the experimentally sampled regions should be taken with some caution, but this result suggests a composition space worthy of future investigation.

For the RS analysis of the a-SiN_x:H ILD etch rate, a much higher R^2 value of 0.97 was obtained, indicating that the model fitted 97% of the observed variability in etch rate. The RS contour profile [Fig. 6(b)] captures the trends observed in Fig. 5, where ILD etch rate increases as a function of both hydrogen content and N/Si ratio. This is consistent with the RS model where %H, Si, and N were all found to be stronger effects than any cross term interactions. For the ILD a-SiN_x:H etch rate, the predicted maximum etch rate is centered at 100% H and broadly decreases as one moves toward the Si-N tie-line with a minimum predicted at predominantly silicon-rich conditions [see Fig. 6(b)]. This visually indicates that, within the film-forming regions of the Si-N-H system, hydrogen content and silicon content are the dominating factors for determining the a-SiN_x:H ILD etch rate.

13 November 2025 14:59:35

Micron Ex. 1032, p. 9
Micron v. YMTC
IPR2025-00117

3. a-SiC$_x$:H

Figure 7 presents the ES and ILD etch rates for the a-SiC$_x$:H films investigated in this study as a function of both hydrogen content and C/Si ratio, x. As shown in Fig. 7(a), the a-SiC$_x$:H ES and ILD etch rates were both quite low at 2–3 Å/s for <45% H. However, the ES etch rate showed a huge variance (~2–55 Å/s) for films with hydrogen content of 45%–55%, while the ILD etch rate remained relatively unchanged as hydrogen content increased further. The ES etch rates can be better understood by looking at their dependence on C/Si ratio. As Fig. 7(b) shows, the increase in ES etch rate for films with >45% hydrogen content corresponds directly with a shift in the C/Si ratio away from the stoichiometric value of 1.0 to higher values. In fact, the a-SiC$_x$:H etch rate is observed to increase almost linearly with x from 1 to 4.5. With increasing carbon content, carbon becomes increasingly incorporated as terminal CH_3 groups instead of in a network-forming capacity where C is predominantly bound to C and Si atoms and hydrogen predominantly incorporated as monohydrides (C–H and Si–H).[85,86] In the latter case, three or four Si–C or C–C bonds must be broken in order for a Si or C atom to be removed from the material. However, for the terminal CH_3 species, only a single Si–C or C–C bond must be broken in order for a carbon atom to be removed from the material.

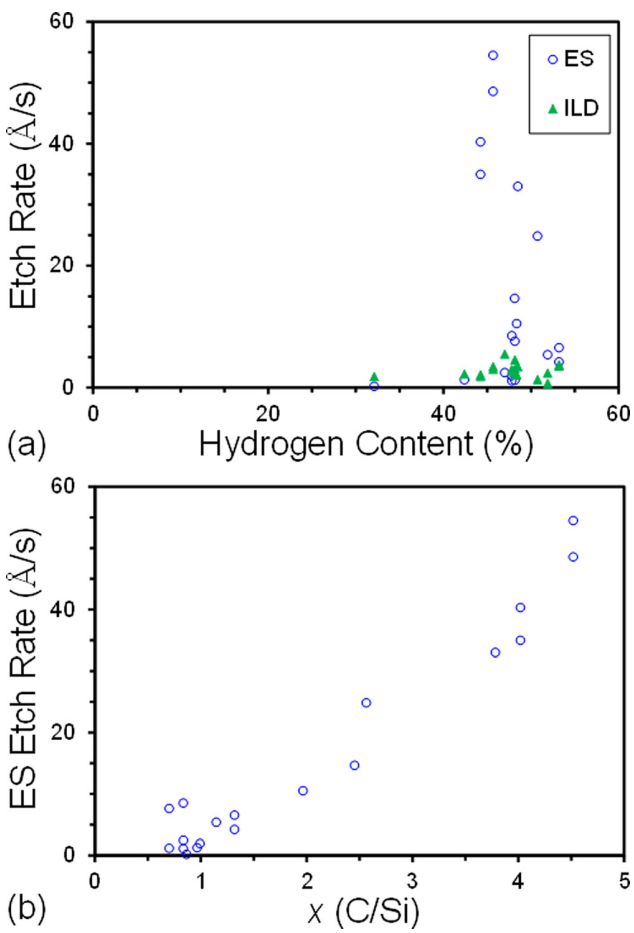

FIG. 7. (Color online) (a) ES and ILD etch rates for a-SiC$_x$:H as a function of hydrogen content (%), (b) a-SiC$_x$:H ES etch rates as a function of x (C/Si).

The amount of interconnected nanoporosity was also observed to increase substantially for SiC$_x$:H films with H > 45% and C/Si > 1,[59] coincident with environmental oxygen contamination increasing to as high as 15–18%. These factors likely also contribute to the enhanced ES etch rate for the highest carbon content a-SiC$_x$:H films due to deeper penetration into the surface of the films by the plasma-activated reactants generated in the CF_4/O_2 plasma. This is illustrated in Fig. 8 where the a-SiC$_x$:H ES etch rates are plotted as a function of mass density. Here, one can see a gradual increase in etch rate with decreasing mass density similar to that observed for a-C:H. One can also observe that the films with significant amounts of interconnected nanoporosity exhibit significantly higher etch rates relative to those with similar mass densities. This effect will be even more clearly shown later in the examination of the a-SiO$_x$C$_y$:H system.

For the ILD etch, the a-SiC$_x$:H etch rate essentially shows no dependence on hydrogen (or carbon) content, and the measured etch rates were quite low (<5 Å/s) for the composition space examined. This is consistent with the generally low to negligible etch rates observed for single-crystalline SiC in fluorinated plasmas[87] and the similarly low etch rates observed for a-SiC:H.[41] For highly polymerizing fluorinated plasmas (such as CHF_3), the low etch rates have been directly attributed to the growth of a relatively thick CF$_x$ surface layer on a-SiC:H.[41,43,44]

To more clearly visualize the interplay between Si, C, and H content on the ES and ILD etch rates, a response surface analysis on the a-SiC$_x$:H system was also performed. The resulting ES and ILD etch rate ternary contour plots predicted from the RS model are shown in Fig. 9. As for the a-SiN$_x$:H system, the previously presented results for a-Si, a-Si:H, and a-C:H were included to allow the Si-C-H composition space to be more fully sampled and improve the coverage of the RS analysis. Similarly, the triangle of open circles in the hydrogen-rich portion of the Si-C-H composition demarcates the region where topological constraint theory[82,83] indicates continuously networked films are unlikely.

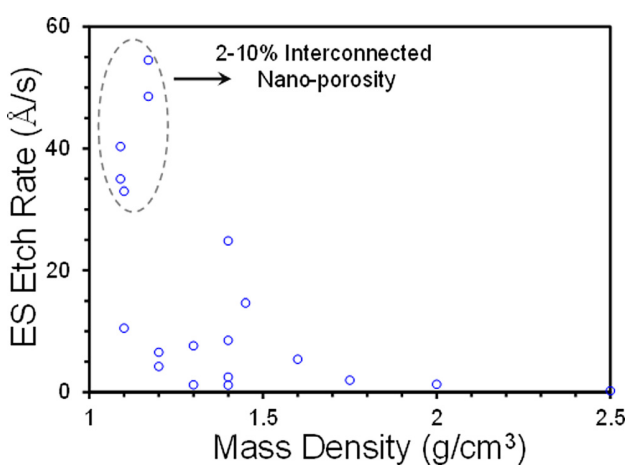

FIG. 8. (Color online) a-SiC$_x$:H ES etch rates as a function of mass density.

13 November 2025 14:59:35

Micron Ex. 1032, p. 10
Micron v. YMTC
IPR2025-00117

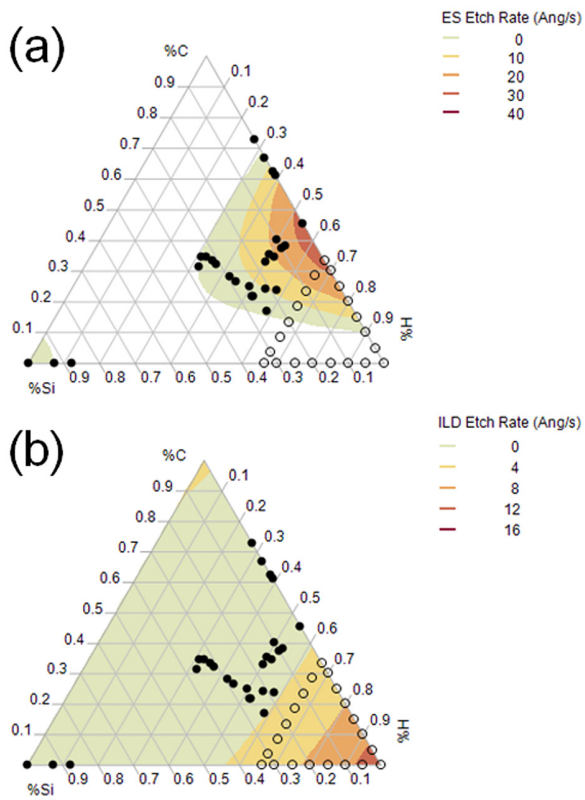

FIG. 9. (Color online) (a) ES and (b) ILD etch rates for a-SiC$_x$:H as a function of silicon, carbon, and hydrogen content (%). Filled circles represent experimental data points and open circles non-film-forming compositions.

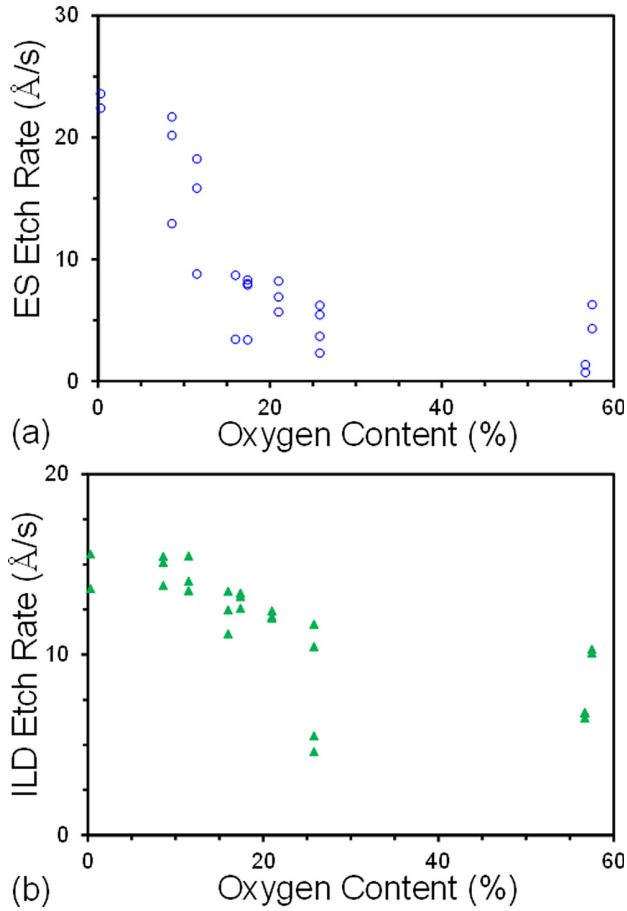

FIG. 10. (Color online) (a) ES and (b) ILD etch rates for a-SiO$_x$N$_y$:H as a function of oxygen content (%).

For the RS analysis of the a-SiC$_x$:H ES etch rate, an R^2 value of 0.60 was obtained, indicating that only 60% of the observed variability in etch rate was captured by the RS model. This could be due to the incomplete coverage of the full Si-C-H composition space and/or the additional nonlinear effect resulting from the presence of nanoporosity which is not explicitly a function of elemental composition. We do note that the near zero etch rates predicted for the low hydrogen content composition space is consistent with the comparatively low CF_4/O_2 etch rates reported in the literature for single crystal SiC (Ref. 87) and diamond.[88] However, contour plots in Fig. 9(a) do reasonably capture that beyond ~20% H, the a-SiC$_x$:H ES etch rate clearly increases with increasing carbon content, reaching values of ≥40 Å/s. The RS contour plots also capture the a-C:H etch rate increasing with increasing hydrogen content.

For the RS analysis of the a-SiC$_x$:H ILD etch rate, a low R^2 value of 0.30 was obtained, indicating a poor fit to the experimental data. This is likely due to the low and generally unvarying ILD etch rates measured for all the a-SiC$_x$:H samples. However, the RS contour plot displayed in Fig. 9(b) does capture qualitatively the lack of variability in ILD etch rate in the Si-C-H system.

4. a-SiO$_x$N$_y$:H

Figure 10 presents the ES and ILD etch rates for a series of a-SiO$_x$N$_y$:H films produced by intentionally adding an oxidizer to the deposition chemistry for one of the a-SiN$_x$:H films examined in Sec. III B 2. This generated films with oxygen content up to ~30% while hydrogen content remained relatively constant at 18%–20%. To illustrate how the a-SiO$_x$N$_y$:H etch rates compare with those for zero nitrogen content, etch results for two PECVD SiO_2 films were included in Fig. 10 that had 7%–14% hydrogen and trace (but detectable) N levels of 0%–5%. As can be seen, both the ES and ILD etch rates for the a-SiO$_x$N$_y$:H films smoothly decreased with increasing oxygen content to values approaching those for a-SiO_2. For the ES etch, the a-SiO$_x$N$_y$:H etch rate quickly approached the values measured for PECVD SiO_2 at 20%–30% oxygen. For the ILD etch, the a-SiO$_x$N$_y$:H etch rate decreased to the PECVD SiO_2 values in a more linear fashion.

Several prior studies have investigated the influence of O/N content on a-SiO$_x$N$_y$:H etch rates in various dry plasmas.[89–92] Of particular relevance to this study is the investigation by Cavallari and Gualandris where CF_4/O_2 dry etch rates as a function of PECVD a-SiO$_x$N$_y$:H RI were reported.[89] In this study, the authors observed that etch rate increased smoothly as RI increased from 1.4 (for SiO_2) to 1.6 (for oxygen-rich a-SiO$_x$N$_y$:H), while reaching a plateau at RI values of 1.8–1.9 (nitrogen-rich a-SiO$_x$N$_y$:H). These results are in excellent agreement with those reported here for a-SiO$_x$N$_y$:H CF_4/O_2 etching where etch rate was also observed to increase with

13 November 2025 14:59:35

Micron Ex. 1032, p. 11
Micron v. YMTC
IPR2025-00117

decreasing oxygen content and increasing RI (not shown). In contrast, Ueno *et al.* investigated CHF_3 reactive ion etching of PECVD a-SiO_xN_y:H and observed that the dry etch rate increased slightly as RI decreased from 2.1 to 1.6 and plateaued at a RI value of 1.44 (i.e., for SiO_2).[90] However, the counter trend observed by Ueno can be partly explained by the fact that the starting base a-SiN_x:H film was Si-rich with $x \cong 0.6$, whereas x for the starting a-SiN_x:H film in this study was closer to 1.0.

To help better understand how the exact elemental composition in the Si-O-N system can influence dry etch rates, we present in Fig. 11 ternary Si-O-N RS contour plots for ES and ILD etch rates based on the a-SiO_xN_y:H films investigated in this study. The plots are valid only for $H \leq 20\%$, and can more accurately be viewed as a slice through a Si-O-N-H pyramidal quaternary diagram at $H \sim 20\%$. However, we believe Fig. 11 should still be predictive of general trends for other hydrogen contents reasonably outside this narrow range of H. As for the previous ternary diagrams, the open circles represent known non-film-forming regions, which in this case essentially encompass the entire O–N axis and surrounding region (i.e., O_2, N_2, N_2O and similar species are all gases at room temperature). The R^2 for both the ES and ILD etch RS models were high at 0.8 and 0.9, respectively, and the predicted response surface contour plots reproduce well the behavior shown in Fig. 10 where increasing oxygen content for a a-SiN_x:H film with $x = 1$ leads to a decrease in both the ES and ILD etch rates. In addition, Fig. 11(b) shows that the addition of oxygen to a a-SiN_x:H film with $x = 0.6$ (i.e., >65% Si) can lead to a slight increase in ILD etch rate as observed in the Ueno study.[90]

5. a-SiC_xN_y:H

For the a-SiC_xN_y:H system, only a limited number of samples with compositions within the Si-C-N ternary system were obtained (see Table I), which exhibited high ES etch rates of ~50 Å/s and moderate ILD etch rates of ~5 Å/s. Despite the limited composition space for the SiC_xN_y:H samples, when included with samples from the previously presented Si-N-H and Si-C-H systems, a reasonable response surface analysis of the Si-C-N system was possible. As Secs. III B 1–III B 4 have shown that high hydrogen content and interconnected porosity can significantly influence both the ES and ILD etch rates, the merged a-Si:H, a-C:H, a-SiN_x:H and a-SiC_x:H datasets were intentionally limited to samples with hydrogen content <50% where interconnected porosity was observed to develop in a-C:H and a-SiC_x:H. The resulting Si-C-N ternary ES ($R^2 = 0.8$) and ILD ($R^2 = 0.9$) etch rate RS contour plots are both shown in Fig. 12. For the ES etch rate, a predicted maximum exists along the C-N tie-line at approximately 45% N. This maximum decreases with increasing Si content along a ridge that follows a tie-line to roughly 85% Si on the Si-N tie-

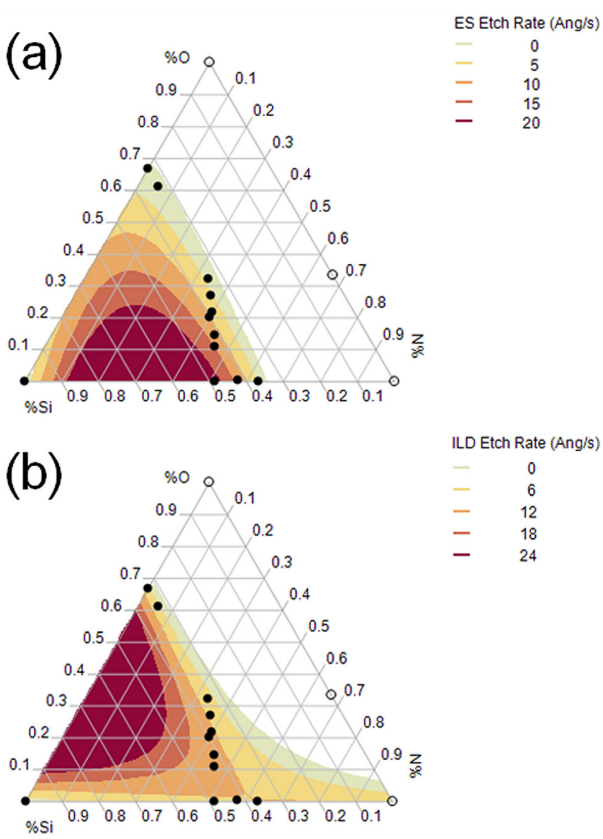

FIG. 11. (Color online) (a) ES and (b) ILD etch rates for a-SiO_xN_y:H as a function of silicon, oxygen and nitrogen content (%). Filled circles represent experimental data points and open circles non-film-forming compositions.

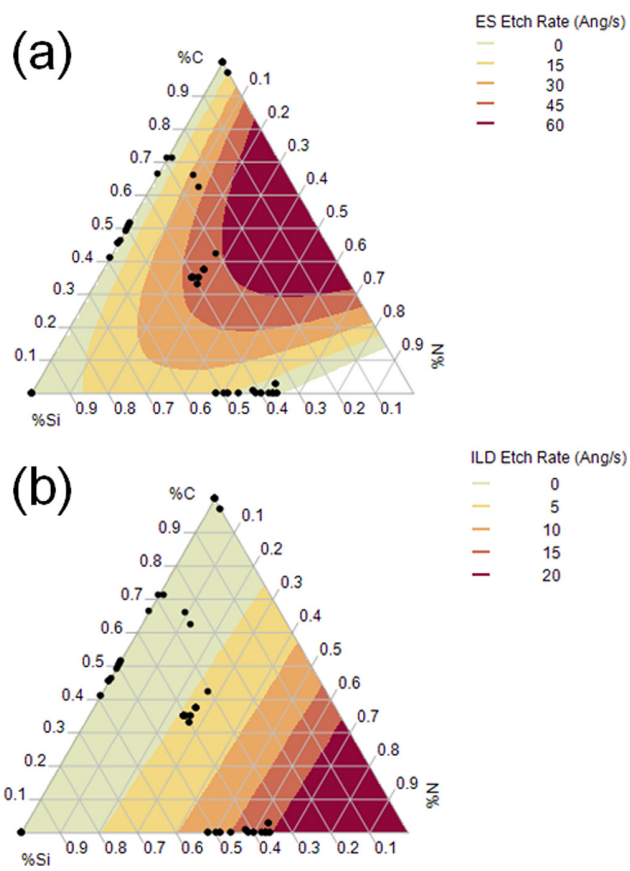

FIG. 12. (Color online) (a) ES and (b) ILD etch rates for a-SiC_xN_y:H as a function of silicon, nitrogen, and carbon content (%).

13 November 2025 14:59:35

Micron Ex. 1032, p. 12
Micron v. YMTC
IPR2025-00117

line. Interestingly, the predicted maximum corresponds to an approximately stoichiometric C_3N_4 composition, and may represent a material class worthy of further investigation in this regard. This maximum is somewhat similar to the maximum observed along the C-H tie-line in the Si-C-H system and suggests that the addition of nitrogen to carbon could play a similar role in reducing network connectivity and developing nanoporosity.

In contrast, the ILD etch rates show a maximum that falls within the nitrogen-rich phase field and decreases with increasing Si and/or C content at a similar rate. In this regard, we do note that while constraint theory would predict that continuous networked films are possible in the nitrogen-rich composition space, pure (100%) nitrogen is a gas (i.e., N_2). As both the predicted maxima also fall outside the composition range sampled for this ternary system, we note that some caution should be taken in these extrapolated results despite the high R^2 for the RS model.

As mentioned previously, hydrogen has been shown to have a significant influence on both the ES and ILD etch rates in a-SiN_x:H and a-SiC_x:H. Thus, it can be anticipated that hydrogen content variations would also have a similar effect within the a-SiC_xN_y:H system. In this regard, we can envision a three dimensional quaternary plot with hydrogen represented by an apex extending out of the plane for the Si-C-N ternary plots shown in Fig. 12. Two of the faces of this pyramid are represented by the Si-N-H and Si-C-H ternary plots shown in Figs. 7 and 10, respectively, and the third by a similar C-N-H ternary plot not directly investigated in this study due to the unavailability of a-CN_x:H samples. Figure 12 can thus be considered as a top-down view of this pyramid where the top hydrogen rich portion of the quaternary pyramid has been removed. Based on this perspective and the trends observed for a-SiN_x:H and a-SiC_x:H systems, we would anticipate that the contour plot for the ES etch rate quaternary would show a maximum along the C-H tie-line that decreases/slopes toward the Si-N tie-line. Similarly for the ILD etch rate quaternary, we would anticipate a maximum along the N-H tie-line that decreases/slopes toward the Si-C tie-line.

6. a-SiO_xC_y:H

The final ternary composition space examined is the SiO_xC_y:H system. Due to the widely varying ways that these films may be fabricated and that carbon may be incorporated into the SiO_2 network and produce different degrees of isolated and interconnected nanoporosity,[93,94] this is the most complex system to interpret and explain the observed etch rate behavior. It is also arguably the most well-studied of the material subclasses, and therefore, a lot is known regarding the atomic structure for various compositions and fabrication methods. To assist the interpretation and allow various trends to be more clearly observed, we classify the a-SiO_xC_y:H films based on whether the network bonding is predominantly Si–O (i.e., a-SiOC:H) or Si–C and Si–O (i.e., a-SiCO:H) and whether the films contain significant levels of interconnected porosity (typically >12% porosity with pore diameter >1 nm). The former classification is based on transmission Fourier transform-infrared spectroscopy measurements and the latter based on both ellipsometric porosimetry and positronium annihilation lifetime spectroscopy measurements that have all been previously described in detail.[58]

Figure 13 presents the a-SiO_xC_y:H ES etch rates as a function of both carbon and hydrogen content. A general increase in etch rate with both increasing carbon and hydrogen content was observed. This trend is consistent with prior observations for other systems (i.e., a-C:H, a-SiO_x:H, and a-SiC_x:H) where increasing hydrogen/terminal CH_x content was observed to lead to an increased ES etch rate. For a-SiO_xC_y:H, the connection between carbon and hydrogen content both increasing in concert is similar to that for a-SiC_x:H where for PECVD a-SiO_xC_y:H hydrogen is in many cases also predominantly coincorporated with carbon as terminal CH_x groups.[93,94]

Focusing on Fig. 13(a) in more detail, one can observe more subtle differences in etch rate. Relative to pure PECVD SiO_2, the incorporation of even trace (1%–4%) amounts of carbon was observed to result in a two-to-threefold increase in the ES etch rate. However, for increasing levels of carbon, the ES rate was either further increased or reduced depending on the way in which the carbon was incorporated into the

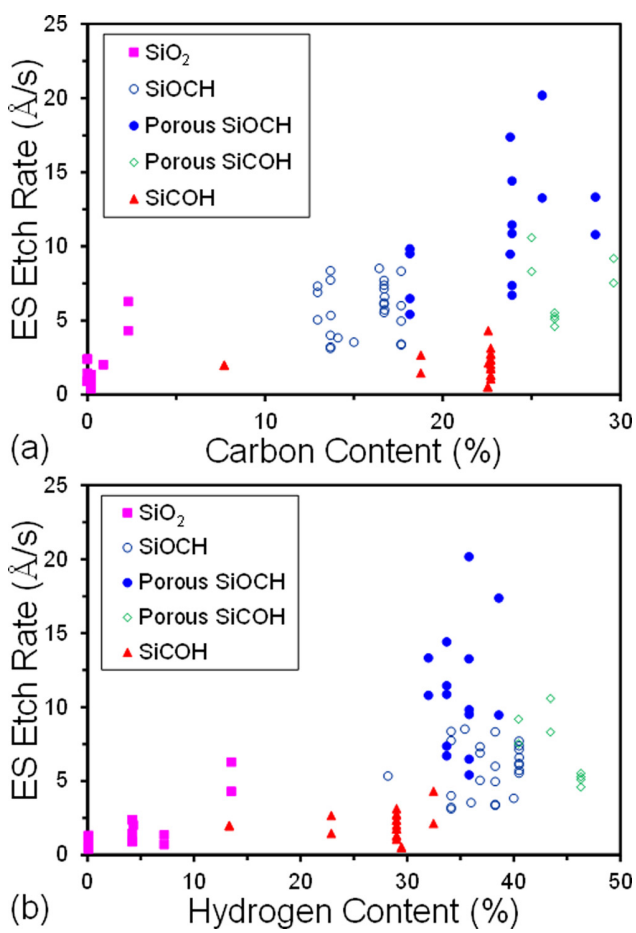

FIG. 13. (Color online) ES etch rates for a-SiO_xC_y:H as a function of (a) carbon content (%), and (b) hydrogen content (%).

13 November 2025 14:59:35

Micron Ex. 1032, p. 13
Micron v. YMTC
IPR2025-00117

films. For the a-SiO_xC_y:H films with small amounts of carbon (12%–17%), the carbon was predominantly incorporated as terminal CH_x groups that lower the density of the material and increase both the size and amount of nanopores present in the material (see data points labeled SiOCH).[93,94] When the concentration of carbon incorporated as terminal CH_x groups increases beyond 18%, the nanopores present in these materials start to become interconnected, which results in a highly porous material.[58] As previously observed for both a-C:H and a-SiC_x:H, this leads to further increases in a-SiO_xC_y:H etch rate due to both the lower mass density and the ability of the plasma-generated etch precursors to penetrate more deeply into the surface of the a-SiO_xC_y:H film (see porous SiOCH data points). This latter point is more clearly observed in Fig. 13(b), in contrasting data points for SiOCH and porous SiOCH, where films with similar hydrogen content but higher levels of interconnected nanoporosity exhibit higher ES etch rates. A similar dependence of etch rate on porosity for low-*k* a-SiOC:H materials has also been observed and reported by others.[95–99]

However, carbon can also be incorporated directly in the network structure of a-SiO_xC_y:H as opposed to as terminal CH_x groups.[61,100] The a-SiO_xC_y:H thin films where carbon was incorporated in this fashion are signified in Fig. 13 as SiCOH and porous SiCOH. As shown in Fig. 13(a), the SiCOH films exhibit very low ES etch rates of 1–4 Å/s and, as illustrated in Fig. 13(b), also exhibit reduced hydrogen content relative to many of the SiOCH class films. Both of these observations are due to these films having both Si–O–Si and Si–C–Si linkages, where for the latter, the carbon is primarily fourfold-bonded to Si.[61] The presence of $C(Si)_4$ groups and the low ES etch rate is thus consistent with the low ES etch rates observed for a-SiC_x:H films with similar hydrogen content.

Films with both Si–O–Si and Si–C–Si linkages and increased hydrogen content can also be made. In this case, the increased hydrogen content leads to the conversion of carbon incorporated primarily as $C(Si)_4$ groups to Si–CH_2–Si groups.[100] As for a-SiC_x:H, this leads to the development of some interconnected nanoporosity.[58] This results in the ES etch rates for the porous SiCO:H films increasing relative to those for nonporous SiCO:H. However, the amount of interconnected nanoporosity in the porous SiCO:H materials is lower than in the porous SiOC:H materials, despite these films in some cases having both higher carbon and hydrogen content. Thus, the ES etch rates for the porous SiCO:H materials are significantly lower than those for porous SiOC:H. This is consistent with several studies of the plasma ash and damage resistance of low-*k* a-SiOC:H and a-SiCO:H where the a-SiOC:H materials that have increased Si–CH_2–Si linkages have been reported to be more resistant to various plasma processes.[101]

For the ILD etch, similar behavior is observed, but the trends are more heavily dominated by how carbon is incorporated in the a-SiO_xC_y:H network rather than the porosity. As shown in Fig. 14, the a-SiO_xC_y:H films wherein carbon is incorporated predominantly as terminal CH_x groups (i.e., SiOCH and porous SiOCH) all exhibit similar ILD etch rates

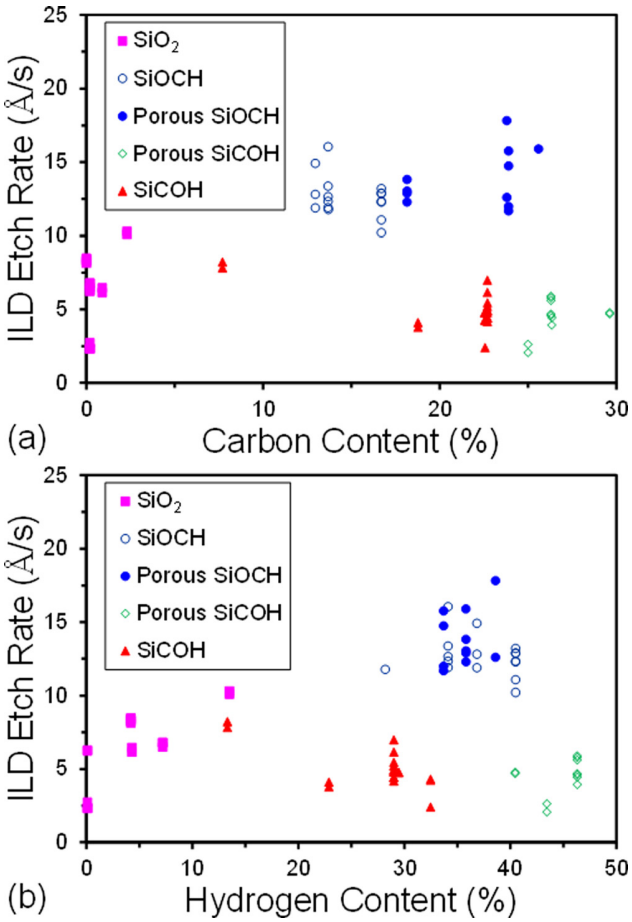

FIG. 14. (Color online) ILD etch rates for a-SiO_xC_y:H as a function of (a) carbon content (%), and (b) hydrogen content (%).

independent of the carbon and hydrogen content. Likewise, a-SiO_xC_y:H films where carbon is more directly a part of the network structure (i.e., SiCOH and porous SiCOH) also exhibit similar (but lower) ILD etch rates independent of the carbon and hydrogen content. This could be a result again of the tendency of the CHF_3 ILD etch plasma to codeposit and form CF_x residues on the a-SiO_xC_y:H surface that partially block nanopores exposed at the surface, thus preventing deeper penetration of the plasma-generated etchants into the film surface.[69,70] However, it has been additionally shown by Standaert that the presence of hydrogen and carbon in silicate glasses can influence and increase the thickness of the surface fluoride layer that develops on the silicate surface during CHF_3 etching.[102]

Although a sufficiently large sample set of a-SiO_xC_y:H samples was investigated in this study, a more detailed RS model for this system was not attempted due to the additional complexity of how carbon was incorporated and the significant influence of extended nanoporosity when present.

C. Identification of alternate etch colors

In order to conclude by identifying possible third or fourth color materials for pitch-division and multipattern processing, we consider a basic dual damascene scheme

13 November 2025 14:59:35

Micron Ex. 1032, p. 14
Micron v. YMTC
IPR2025-00117

utilized for forming trench and via patterns in an ILD material that will be subsequently filled with a metal such as Cu to form a metal interconnect layer.[103] We note that this is just one of many examples where a pitch-division patterning scheme may be utilized and that some details have been omitted to avoid creating a lengthy tutorial. For the specific application described here, SiO_2 or a low-*k* a-SiOC:H dielectric is utilized as the ILD and a thin a-SiN:H or a-SiCN:H layer is typically inserted below the ILD to serve as both an etch stop for the ILD etch, a metal adhesion layer, and a barrier for diffusion into and out of the underlying metal layers.[36] To form such metal interconnect layers, optical lithography techniques are utilized to define patterns in a photoresist material spin-coated on top of the ILD material. This pattern is subsequently transferred directly into the ILD material using a dry anistropic etch and ideally selectively stops within the underlying etch stop layer. To allow connections between the new metal layer and underlying metal layers, additional photolithographical patterning is performed and a second etch (i.e., ES etch) is used to break through the underlying etch stop/adhesion layer/diffusion barrier. Before the trenches and vias are filled with metal, any remaining photoresist not consumed by the ILD and ES etches is subsequently removed by a series of dry plasma ashes and wet cleans. Thus, product requirements (such as the ILD must be an excellent electrical insulator) and integration requirements (such as the ES must also be a good diffusion barrier and adhesion layer to the underlying metal layer) by default specifically define two material and etch combinations (i.e., colors) for this particular patterning scheme (see Fig. 1 of Ref. 103 for more details regarding dual damascene patterning methods).

In more advanced dual damascene patterning schemes, a hardmask material may be added on top of the ILD to, among many additional considerations,[39] improve the pattern transfer fidelity of high aspect ratio features from the photoresist into the underlying ILD.[104] The hardmask in this case is ideally required to be selectively etched relative to the ILD, remain in place during the subsequent ILD and ES etches, and easily removed after completion of the ILD and ES etches. In this regard, such hardmasks represent a need for a third color material and etch combination. For more complex multipattern dual damascene schemes, additional backbone and spacer materials may be added on top of the hardmask that must in turn be selectively etched and removed relative to the underlying hardmask and exposed ILD and ES materials.[23] These backbone and spacer materials thus represent a need for a third or fourth color combination of materials and etches. In even more complex multipatterning schemes, dissimilar etch stop materials may be used to cover different metal lines that require unique etches to selectively breakthrough and etch one ES material in the presence of the others and the ILD material.[33] By default, the additional etch stop materials represent third and fourth color materials that require unique third and fourth color etches.

Consideration of the above dual damascene patterning schemes helps to define the material and etch criteria for potential third and fourth colors. Specifically, any third or fourth color material must have either a zero etch rate in both the ES and ILD etches or several orders of magnitude higher etch rate in these two etches relative to the ES and ILD materials utilized. This in turn requires the identification of a third and fourth color plasma etch that can etch the still-to-be-identified third and fourth color pattern materials but not etch the already defined ES and ILD materials. Although other etch chemistries were not investigated in this study, a number of other dry etch chemistries based on H_2, HCl, Cl_2, CCl_4, HBr, Br_2, BCl_3, NF_3, and SF_6 are available and commonly utilized in the semiconductor industry.[84,105] Thus, the goal of this study is to identify potential materials within the Si-C-O-N-H system that, in combination with these other etches, *may* facilitate third and fourth color patterning.

To help identify potential third and fourth color materials from the Si-C-O-N-H system in the context of the above dual damascene patterning schemes, we summarize in Fig. 15 the ES and ILD etch rates for the various materials examined normalized to the etch rate of a well-known ILD material: SiO_2. The results are again presented as a function of mass density both for clarity of presentation and to more easily facilitate discussion later regarding additional requirements for the various materials. As shown in Fig. 15(a), a wide range of etch

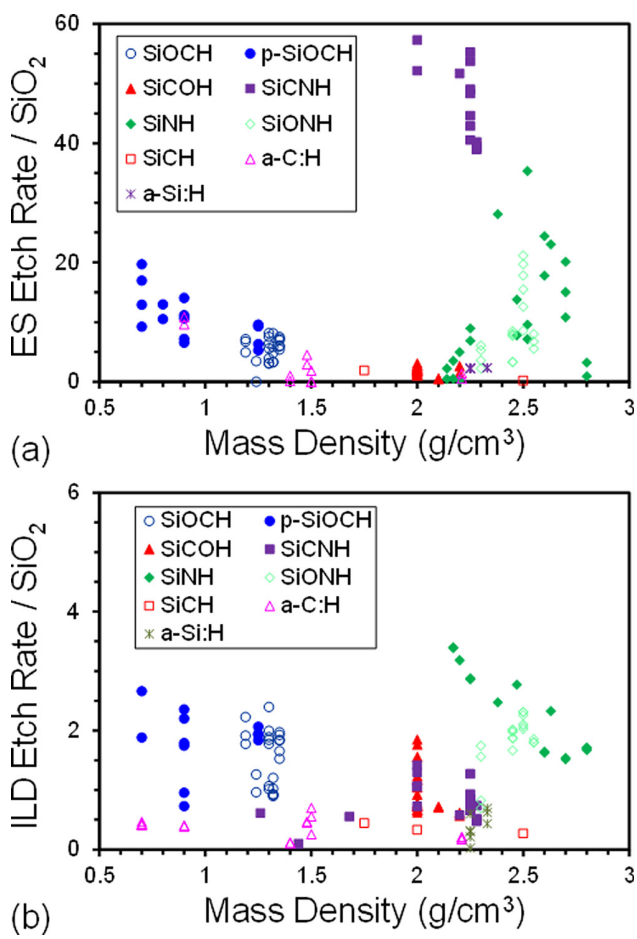

FIG. 15. (Color online) (a) ES etch rates and (b) ILD etch rates for various materials examined in this study relative to a-SiO_2.

13 November 2025 14:59:35

Micron Ex. 1032, p. 15
Micron v. YMTC
IPR2025-00117

rates relative to SiO_2 was observed using the CF_4/O_2 ES etch. As perhaps expected based on the name of the etch, the a-SiN:H and a-SiCN:H materials most commonly used as the etch stop in dual damascene metal interconnect patterning exhibit significantly higher etch rates relative to SiO_2 with etch selectivities as high as ~60:1. This means that after trenches and vias have been properly defined in the ILD, the etch stop materials can be easily etched through to expose the underlying metal layer without significantly etching the ILD material further and inducing a loss in pattern fidelity or critical dimension (CD) control. However, some of this selectivity is lost if low-*k* a-SiOC:H or porous a-SiOC:H (p-SiOC:H) materials are used as the ILD instead of SiO_2 in order to reduce parasitic capacitive delays in the metal interconnect. As shown in Fig. 15(a), the a-SiOC:H and p-SiOC:H materials exhibit higher etch rates in the ES etch relative to SiO_2. Depending on the specific composition of the ILD and ES, the use of low-*k* ILDs can reduce the ES/ILD etch selectivity from as high as 60:1 to as low as 1:1.

From the perspective of identifying potential third and fourth color materials, none of the materials examined in the Si-C-O-N-H system exhibit several order of magnitude higher etch rates in the ES etch relative to SiO_2. SiCN:H exhibits the highest etch selectivity of up to 60:1, and based on response surface modeling of the Si-C-N ternary system, a-CN:(H) may demonstrate even higher etch selectivity than this. On the other hand, several materials exhibit sufficiently low to negligible ES etch rates to merit further consideration. Of these, the high-density/low-hydrogen-content forms of a-C:H, a-Si:H, a-SiC:H, and SiCO:H stand out as well as Si-rich a-SiN_x:H. To further cull this list, we next look at the ILD etch rates of the various examined materials in the CHF_3 ILD etch.

As shown in Fig. 15(b), all the materials exhibit comparable etch rates relative to SiO_2 with etch selectivities ranging from <0.1 to 5, with a-C:H, a-Si:H, a-SiC:H, and a-SiOC:H still exhibiting the lowest relative etch rates. The narrower range in etch selectivity can be attributed to the polymerizing nature of the CHF_3 chemistry that for blanket etch rate measurements can result in the formation of a significant fluorinated polymer surface layer in most cases. Once formed, physical ion bombardment and surface defluorination is required for etching to be sustained and this can reduce/mute the sensitivity between the etch chemistry and the material.[43,44] However, such polymer formation is beneficial in that the polymer buildup that occurs on the sidewalls of an etched feature helps to create the anisotropy needed to transfer high aspect ratio features into the desired material. For ILD etching, this polymer buildup also helps to slow the etch and overcome the low blanket etch selectivity observed between the various SiO_2 and a-SiOC:H ILD materials and a-SiN:H and a-SiCN:H ES materials shown in Fig. 15(b).[36,105]

At this point, we do note that the etch selectivities presented in Fig. 15 are relevant only to the specific process conditions utilized for the CF_4/O_2 and CHF_3 etches. Numerous studies have shown that widely varying etch rates and etch selectivities can be achieved by varying CF_4/O_2 ratios, pressure, power, bias, and numerous other process conditions.[89,95–99] Thus, it is possible that for a given combination of materials, significantly better (or worse) etch selectivities may be achieved by using different process conditions or slightly different process chemistries (i.e., CH_2F_2, CF_4/Ar, C_2F_6/O_2, etc.).[42–44,106,107] However, tweaking process conditions by ±10%–50% (as in a typical plasma etch design of experiments[72,108]) is not likely to manipulate etch selectivities by the several orders of magnitude needed to by itself create a third or fourth color material from the Si-C-O-N-H system. In this regard, we believe that materials that show near negligible etch rates in both the CF_4/O_2 ES and CHF_3 ILD etches will hold the most promise as candidate third and fourth color materials from the Si-C-O-N-H system.

In this regard, the high-density/low-hydrogen-content a-C:H, a-Si:H, and a-SiC:H films show the most promise as potential third and fourth color materials. For the latter, Posseme and Standaert have both investigated in detail the etch selectivity of a-SiC:H relative to SiO_2, a-SiOC:H, and a-SiN:H and confirmed that a-SiC:H has low etch rates and high etch selectivity in a variety of fluorinated plasma etch chemistries including CF_4, CHF_3, C_4F_8, CH_2F_2, and C_4F_6.[43,44] Based on this, one would anticipate that a-SiC:H could represent a potential third color patterning material. However, investigations of a-SiC:H as a hardmask in low-*k*/Cu dual damascene patterning by Darnon concluded that a-SiC:H did not have sufficient etch selectivity.[104] Although the technical details of the a-SiC:H were not reported by Darnon, it is possible that the a-SiC:H utilized in this study was a low-density/high-hydrogen-content material. For the a-SiC:H utilized by the same group in the Posseme study, a mass density of 2.0 g/cm^3 and hydrogen content of 50% was reported.[43] As this study has demonstrated, the etch resistance of a-SiC:H in both ES and ILD etches can be dramatically improved by reducing hydrogen content down to 25% to achieve mass densities of 2.5 g/cm^3 or greater. Therefore, reconsideration of higher density/lower hydrogen content a-SiC:H as a hardmask or other patterning material may be merited, but will require the identification of non-fluorine-based dry etch chemistries to enable selective dry patterning of a-SiC:H as well as wet chemical or other routes for a-SiC:H hardmask removal after the patterning process has been completed. The latter has been demonstrated for lower density forms of a-SiC:H,[109] but may be more challenging for higher density/lower hydrogen content forms of a-SiC:H.[110]

The challenges of etching high-density/low-hydrogen-content a-SiC:H may make a-C:H and a-Si:H more attractive as potential third/fourth color pattern materials from the Si-C-O-N-H system. Numerous methods for wet and dry etching of both materials are known,[111,112] and the use of various forms of both as hardmasks has already been reported.[113–116] The primary challenge with using a-C:H as a hardmask that limits its consideration as a possible third color pattern material concerns differentiation between a-C:H and photoresist. Specifically, the O_2 and H_2 based plasmas typically utilized to dry etch and pattern a-C:H can also aggressively attack photoresist.[117] These etches are also problematic when used

13 November 2025 14:59:35

Micron Ex. 1032, p. 16
Micron v. YMTC
IPR2025-00117

for patterning low-*k* a-SiOC:H dielectrics due to their propensity to selectively remove carbon from low-*k* materials and create a host of performance and reliability issues.[118] Optical transparency can also be a major challenge for both a-C:H and a-Si:H.[114] However, this is a challenge for other commonly used hardmask materials such as TiN as well.[37]

Beyond blanket hardmask applications, use of a-C:H, a-Si:H, and a-SiC:H as backbone and/or spacer materials in multipatterning approaches may be limited by additional requirements beyond etch selectivities. As one example, spacer materials utilized in multipatterning processes must have high conformality and step coverage while having low deposition temperatures compatible with the melting point of the photoresist material that they may be deposited over.[119] For the CVD and PECVD methods most commonly utilized to deposit these materials, meeting both of these requirements can be a challenging task.[36] Atomic layer deposition (ALD) is one method that has shown the potential to meet these requirements for oxide materials, but viable ALD processes for a-C:H, a-Si:H, and a-SiC:H have so far yet to be demonstrated.[120]

Beyond the above discussion, we acknowledge that many additional factors come into consideration when selecting and optimizing materials and etches to support various patterning schemes. Factors such as line edge roughness, microtrenching, surface roughening, across wafer etch and CD uniformity, cost, defects and environmental-health-safety issues can further constrain and limit the selection process for identifying third and fourth color pattern assist materials and etches.[35,103] Such considerations are beyond the scope of this relatively simple attempt to screen a diverse array of materials based on two common ILD and ES etches. However, as noted previously, the presented study should allow a more rational selection of a reduced subset of materials to be selected for more detailed examinations of the material influence on pattern-dependent etch features.

In this regard, we do note that the carbon-nitrogen-hydrogen system (i.e., a-CN_x:H) is one composition space neglected in this study that has shown promise for developing tribological coatings for magnetic memory devices.[121] Although the response surface modeling of the Si-C-N system performed in this investigation does not suggest this composition space will yield potential third or fourth color materials, the development of such materials could bring additional flexibility and depth to the list of available pattern assist materials. Nevertheless, new materials outside the Si-C-O-N-H system will likely be required to achieve the ultimate goal of true four color patterning. As mentioned previously, TiN is one material outside the Si-C-O-N-H system that has found extensive use as a hardmask material in advanced patterning schemes,[37] but has limitations in terms of defects, optical transparency, and inducing mechanical instabilities in the patterning stack.[38,39] In a follow on article to this one,[56] we explore additional materials outside the Si-C-O-N-H system that offer the potential to be viable third and fourth colors, including high-*k* dielectric (Al_2O_3, AlN, HfO_2) and up-and-coming boron-containing low-*k* dielectric materials (a-B:H, a-BC:H, a-BN:H, and a-BP). As we will show in this second article,[56] these materials offer the potential to bring additional flexibility in the ultimate selection of materials and design of the pitch division pattern stacks.

IV. SUMMARY AND CONCLUSIONS

Two dry fluorinated plasma etches commonly utilized to selectively etch ILD (CHF_3) and ES (CF_4/O_2) materials in dual damascene patterning processes were utilized to survey the etch characteristics of a large array of materials from within the Si-C-O-N-H system to identify possible third and fourth color materials for use in advanced pitch division and multipatterning processes. The materials surveyed exhibited a wide range of relative etch rates in the CF_4/O_2 ES etch with common a-SiCN:H ES materials exhibiting etch selectivities as large as 60:1 and lower than 1:0.1 relative to SiO_2. In contrast, the observed range of etch rates for the CHF_3 ILD etch was reduced with typical ILD to ES etch selectivities ranging from 5:1 to 1:0.1 or less. The reduced range of etch rates observed for the CHF_3 ILD etch was attributed to the tendency of this chemistry to form fluorinated surface layers that required ion-bombardment-induced defluorination to drive further etching.

Both hydrogen and carbon incorporation were found to significantly influence the etch rates of the material classes investigated. Hydrogen was found to increase the dry etch rate of many of the materials by reducing both the atomic density and overall network connectivity. This was not the case, however, in some of the ILD etches due to the aforementioned formation of CF_x surface layers, or in the case of the SiN:H ES etch rates, where the correlation between etch rate and N/Si ratio was the dominant influence. The incorporation of carbon was found to increase or decrease the etch rate of materials depending on how the carbon was incorporated in the film. When carbon was incorporated directly into the network bonding of a material, the etch rates generally decreased or remained low. However, when carbon was incorporated primarily as terminal organic groups (typically CH_3), the etch rates increased following the trends for hydrogen. Further, incorporation of sufficiently large amounts of terminal organics resulted in the development of interconnected porosity and further increases in etch rate. By incorporating oxygen into SiN_x:H to yield SiO_xN_y:H films, both ES and ILD etch rates could be varied smoothly from SiN_x:H ranges to SiO_2 ranges.

Of all the materials examined, high-density/low-hydrogen-content a-C:H, a-Si:H, and a-SiC_x:H exhibited low to negligible etch rates in both the ILD CHF_3 and ES CF_4/O_2 etches and could represent potential third and fourth color patterning assist materials in combination with other still-to-be-determined etches. Beyond these materials, a-CN_x:H represents a composition space that has largely been ignored for patterning applications, but was predicted to exhibit very high (higher than a-$SiCN_x$:H) ES etch rates based on response surface modeling of the Si-C-N ternary system, and may warrant further investigation. It is likely that many more additional considerations beyond those examined in this study will need to be addressed to solidify the selection

13 November 2025 14:59:35

Micron Ex. 1032, p. 17
Micron v. YMTC
IPR2025-00117

of the identified materials as potential third and fourth color materials. It is also likely that many more additional materials (and etches) will need to be identified to provide the flexibility of meeting not only the requirements of multipatterning processing, but the device and product integration requirements. In this regard, we hope that this relatively simple demonstration inspires future united combinatorial material composition and dry etch process chemistry studies. Additional efforts by the authors to perform a similar survey on materials outside the Si-C-N-O-H system including high-*k* (Al_2O_3, AlN, and HfO_2) and boron-containing low-*k* dielectrics (a-B:H, a-BC:H, a-BN:H, and a-BP) will be presented in a companion article to this one.[56]

ACKNOWLEDGMENTS

The authors would like to acknowledge Ebony Mays, Jeff Bielefeld, Canay Ege, Jason Klaus, Ahmad Al-kukhun, John Brooks, Asad Iqbal, Sreenivas Kosaraju, Prahalad Parthangal, David Michalak, Boyan Boyanov, Andy Antonelli, Elizabeth Mallon, and Ramanam Chebiam of Intel Corporation for their assistance in providing various low- and high-*k* dielectric materials for examination in this study. The authors would also like to acknowledge Aman Haque of Penn State University for supplying the CVD Si_3N_4 sample. Assistance with the statistical response surface analysis provided by Georgia Morgan of Intel is also noted and greatly appreciated. UMKC acknowledges financial support from Intel Corporation (Contract No. 2012-IN-2313) and the Defense Threat Reduction Agency (Grant No. HDTRA1-15-1-0020).

[1]G. Moore, Proc. IEEE **86**, 82 (1998).
[2]C. Mack, IEEE Spectrum **52**, 31 (2015).
[3]R. Dennard, F. Gaensslen, H. Yu, V. Rideout, E. Bassous, and A. LeBlanc, IEEE J. Solid-State Circuits **9**, 256 (1974).
[4]S. King, H. Simka, D. Herr, H. Akinaga, and M. Garner, APL Mater. **1**, 040701 (2013).
[5]C. Liu, M. Ostling, and J. Hannon, MRS Bull. **39**, 658 (2014).
[6]C. Mack, J. Micro/Nanolithogr. MEMS, MOEMS **12**, 030101 (2013).
[7]G. Wilk, R. Wallace, and J. Anthony, J. Appl. Phys. **89**, 5243 (2001).
[8]J. Robertson, Rep. Prog. Phys. **69**, 327 (2006).
[9]B. Doyle *et al.*, IEEE Electron Device Lett. **24**, 263 (2003).
[10]K. Kuhn, Microelectron. Eng. **88**, 1044 (2011).
[11]S. Gupta, V. Moroz, L. Smith, Q. Lu, and K. Saraswat, IEEE Trans. Electron Devices **61**, 1222 (2014).
[12]K. Bernstein, R. Cavin, W. Porod, A. Seabaugh, and J. Welser, Proc. IEEE **98**, 2169 (2010).
[13]D. Nikonov and I. Young, Proc. IEEE **101**, 2498 (2013).
[14]Y. Borodovsky, Proc. SPIE **6153**, 615301 (2006).
[15]C. Mack, *Fundamental Principles of Optical Lithography: The Science of Microfabrication* (Wiley, West Sussex, 2007).
[16]*International Technology Roadmap for Semiconductors (ITRS): 2013* (Semiconductor Industry Association, San Jose, CA, 2013).
[17]A. Mallik *et al.*, Proc. SPIE **8679**, 86792Y (2013).
[18]B. Wu and A. Kumar, Appl. Phys. Rev. **1**, 011104 (2014).
[19]R. Peeters *et al.*, Proc. SPIE **9048**, 90481J (2014).
[20]B. Lin, Microelectron. Eng. **143**, 91 (2015).
[21]X. Ma and G. Arce, *Computational Lithography* (Wiley, Hoboken, NJ, 2010).
[22]H. Hody, V. Paraschiv, D. Hellin, T. Vandeweyer, G. Boccardi, and K. Xu, J. Micro/Nanolithogr. MEMS MOEMS **14**, 014504 (2015).
[23]J. Chawla *et al.*, Proc. SPIE **9054**, 905404 (2014).
[24]H. Kim, S. Park, and W. Hinsberg, Chem. Rev. **110**, 146 (2010).
[25]D. Herr, J. Mater. Res. **26**, 122 (2011).
[26]M. Fang and J. Ho, ACS Nano **9**, 8651 (2015).
[27]N. Kihara *et al.*, J. Micro/Nanolithogr. MEMS, MOEMS **14**, 023502 (2015).
[28]F. Hashemi, C. Prasittichai, and S. Bent, ACS Nano **9**, 8710 (2015).
[29]C. Ellinger and S. Nelson, Chem. Mater. **26**, 1514 (2014).
[30]W. Gao, I. Ciofi, Y. Saad, P. Matagne, M. Bachmann, W. Gillijns, K. Lucas, W. Demmerle, and T. Schmoeller, J. Micro/Nanolithogr. MEMS, MOEMS **15**, 013505 (2016).
[31]M. Gardner, "The four color map theorem," in *Sphere Packing, Lewis Carroll, and Reversi* (Cambridge University, New York, 2009).
[32]R. Wilson, *Four Colors Suffice: How the Map Problem was Solved* (Princeton University, Princeton, 2002).
[33]C. Carver, J. Plombon, P. Romero, S. Suri, T. Tronic, and R. Turkot, Jr., ECS J. Solid State Sci. Technol. **4**, N5005 (2015).
[34]S. Yamauchi, A. Hara, K. Oyama, S. Natori, M. Yamato, and H. Yaegashi, Proc. SPIE **8682**, 86821D (2013).
[35]V. Donnelly and A. Kornblit, J. Vac. Sci. Technol., A **31**, 050825 (2013).
[36]S. King, ECS J. Solid State Sci. Technol. **4**, N3029 (2015).
[37]M. Darnon, T. Chevolleau, D. Eon, L. Vallier, J. Torres, and O. Joubert, J. Vac. Sci. Technol., B **24**, 2262 (2006).
[38]G. Stan, C. Ciobanu, I. Levin, H. Yoo, A. Myebrs, K. Singh, C. Jezewski, B. Miner, and S. King, Nano Lett. **15**, 3845 (2015).
[39]J.-F. de Marneffe *et al.*, J. Appl. Phys. **118**, 133302 (2015).
[40]Y. Kuo, J. Vac. Sci. Technol., A **8**, 1702 (1990).
[41]M. Baklanov, M. Van Hove, G. Mannaert, S. Vanhaelemeersch, H. Bender, T. Conard, and K. Maex, J. Vac. Sci. Technol., B **18**, 1281 (2000).
[42]X. Hua, X. Wang, D. Fuentevilla, G. Oehrlein, F. Celii, and K. Kirmse, J. Vac. Sci. Technol., A **21**, 1708 (2003).
[43]N. Posseme, T. Chevolleau, O. Joubert, L. Vallier, and P. Mangiagalli, J. Vac. Sci. Technol., B **21**, 2432 (2003).
[44]T. Standaert, C. Hedlund, E. Joseph, G. Oehrlein, and T. Dalton, J. Vac. Sci. Technol., A **22**, 53 (2004).
[45]J. Lee, G. Lee, J. Min, and S. Moon, J. Vac. Sci. Technol., A **25**, 1395 (2007).
[46]C. Li, R. Gupta, V. Pallem, and G. Oehrlein, J. Vac. Sci. Technol., A **34**, 031306 (2016).
[47]A. G. Nagy, J. Electrochem. Soc. **132**, 689 (1985).
[48]R. N. Carlile, V. C. Liang, O. A. Palusinski, and M. M. Smadi, J. Electrochem. Soc. **135**, 2058 (1988).
[49]D. Kim, E. A. Hudson, D. Cooperberg, E. Edelberg, and M. Srinivasan, Thin Solid Films **515**, 4874 (2007).
[50]J. C. Arnold and H. H. Sawin, J. Appl. Phys. **70**, 5314 (1991).
[51]M. Schaepkens and G. Oehrlein, Appl. Phys. Lett. **72**, 1293 (1998).
[52]C. Hedlund, H.-O. Blom, and S. Berg, J. Vac. Sci. Technol., A **12**, 1962 (1994).
[53]P. Bhatnagar, S. Panda, N. L. Edleman, S. D. Allen, R. Wise, and A. Mahorowala, J. Appl. Phys. **101**, 076102 (2007).
[54]M. F. Doemling, N. R. Rueger, and G. S. Oehrlein, Appl. Phys. Lett. **68**, 10 (1996).
[55]G. S. Upadhyaya, J. L. Shohet, and J. B. Kruger, Appl. Phys. Lett. **91**, 182108 (2007).
[56]S. Dhungana *et al.*, "Boron and high-*k* dielectrics: Possible fourth etch stop colors for multi-pattern optical lithography processing," J. Vac. Sci. Technol., A (submitted).
[57]B. French and S. King, J. Mater. Res. **28**, 2771 (2013).
[58]S. King *et al.*, ECS J. Solid State Sci. Technol. **1**, N115 (2012).
[59]S. King *et al.*, J. Non-Cryst. Solids **379**, 67 (2013).
[60]S. King, J. Vac. Sci. Technol., A **29**, 041501 (2011).
[61]S. King, M. French, M. Jaehnig, M. Kuhn, B. Boyanov, and B. French, J. Vac. Sci. Technol., B **29**, 051207 (2011).
[62]S. King, M. French, M. Jaehnig, M. Kuhn, and B. French, Appl. Phys. Lett. **99**, 202903 (2011).
[63]W. Lanford *et al.*, Nucl. Instrum. Methods B **371**, 211 (2016).
[64]SAS, Cary, NC 27513.
[65]M. Brodsky, D. Kaplan, and J. Ziegler, Appl. Phys. Lett. **21**, 305 (1972).
[66]K. Gerstenberg, Colloid Polym. Sci. **268**, 345 (1990).
[67]C. Ye, Z. Ning, T. Wang, X. Yu, and Y. Xin, Thin Solid Films **496**, 221 (2006).
[68]H. Li, J. Knaup, E. Kaxiras, and J. Vlassak, Acta Mater. **59**, 44 (2011).
[69]S. Bailey, E. Mays, D. Michalak, R. Chebiam, S. King, and R. Sooryakumar, J. Phys. D: Appl. Phys. **46**, 045308 (2013).

13 November 2025 14:59:35

Micron Ex. 1032, p. 18
Micron v. YMTC
IPR2025-00117

[70]T. Standaert, E. Joseph, G. Oehrlein, A. Jain, W. Gill, P. Wayner, and J. Plawsky, J. Vac. Sci. Technol., A **18**, 2742 (2000).
[71]A. Sankaran and M. Kushner, Appl. Phys. Lett. **82**, 1824 (2003).
[72]P. Riley, V. Kulkarni, and S. Bishop, J. Vac. Sci. Technol., B **7**, 24 (1989).
[73]L. Pruette, S. Karecki, R. Reif, L. Tousignant, W. Reagan, S. Kesari, and L. Zazzera, J. Electrochem. Soc. **147**, 1149 (2000).
[74]S. Agarwala, O. King, S. Horst, R. Wilson, D. Stone, M. Dagenais, and Y. Chen, J. Vac. Sci. Technol., A **17**, 52 (1999).
[75]W. Pliskin, J. Vac. Sci. Technol. **14**, 1064 (1977).
[76]F. Becker, D. Pawlik, H. Anzinger, and A. Spitzer, J. Vac. Sci. Technol., B **5**, 1555 (1987).
[77]B. E. E. Kastenmeier, P. J. Matuso, and G. S. Oehrlein, J. Vac. Sci. Technol., A **17**, 3179 (1999).
[78]D. R. Sparks, J. Electrochem. Soc. **139**, 1736 (1992).
[79]D. Buttari *et al.*, Appl. Phys. Lett. **83**, 4779 (2003).
[80]P. E. Riley and D. A. Hanson, J. Vac. Sci. Technol., B **7**, 1352 (1989).
[81]Y. Hahn, J. Lee, K. Mackenzie, D. Johnson, S. Pearton, and F. Ren, Solid-State Electron. **42**, 2017 (1998).
[82]J. Phillips and M. Thorpe, Solid State Commun. **53**, 699 (1985).
[83]P. Boolchand and M. Thorpe, Phys. Rev. B **50**, 10366 (1994).
[84]D. Flamm and V. Donnelly, Plasma Chem. Plasma Process. **1**, 317 (1981).
[85]S. King, M. French, J. Bielefeld, and W. Lanford, J. Non-Cryst. Solids **357**, 2970 (2011).
[86]S. King, J. Bielefeld, M. French, and W. Lanford, J. Non-Cryst. Solids **357**, 3602 (2011).
[87]J. Palmour, R. Davis, T. Wallett, and K. Bhasin, J. Vac. Sci. Technol., A **4**, 590 (1986).
[88]H. Shiomi, Jpn. J. Appl. Phys., Part 1 **36**, 7745 (1997).
[89]C. Cavallari and F. Gualandris, J. Electrochem. Soc. **134**, 1265 (1987).
[90]K. Ueno, T. Kikkawa, and K. Tokashiki, J. Vac. Sci. Technol., B **13**, 1447 (1995).
[91]V. Nguyen, S. Burton, and P. Pan, J. Electrochem. Soc. **131**, 2348 (1984).
[92]Y. Yun, S. Park, D. Kim, N. Lee, K. Kim, and G. Bae, J. Vac. Sci. Technol., A **25**, 980 (2007).
[93]N. Tajima, T. Ohno, T. Hamada, K. Yoneda, N. Kobayashi, S. Hasaka, and M. Inoue, Appl. Phys. Lett. **89**, 061907 (2006).
[94]J. Rimsza, L. Deng, and J. Du, J. Non-Cryst. Solid **431**, 103 (2016).
[95]P. Lazzeri, X. Hua, G. Oehrlein, M. Barozzi, E. Iacob, and M. Anderle, J. Vac. Sci. Technol., B **23**, 1491 (2005).
[96]D. Shamiryan, M. Baklanov, S. Vanhaelemeersch, and K. Maex, J. Vac. Sci. Technol., B **20**, 1923 (2002).
[97]T. Ono, H. Takahashi, K. Kinoshita, N. Fujii, N. Hata, and T. Kikkawa, Jpn. J. Appl. Phys., Part 1 **45**, 8873 (2006).
[98]S. Hwang, G. Lee, J. Min, S. Moon, Y. Kim, H. Ryu, Y. Cho, and J. Kim, Jpn. J. Appl. Phys., Part 1 **41**, 5782 (2002).
[99]N. Possemme, T. Chevolleau, O. Joubert, and L. Vallier, J. Vac. Sci. Technol., B **22**, 2772 (2004).
[100]G. Dubois, W. Volksen, T. Magbitang, M. Sherwood, R. Miller, D. Gage, and R. Dauskardt, J. Sol-Gel Sci. Technol. **48**, 187 (2008).
[101]T. Furusawa, D. Ryuzaki, R. Yoneyama, Y. Homma, and K. Hinode, Electrochem. Solid State Lett. **4**, G31 (2001).
[102]T. Standaert, P. Matsuo, S. Allen, G. Oehrlein, and T. Dalton, J. Vac. Sci. Technol., A **17**, 741 (1999).
[103]T. Tatsumi, Appl. Surf. Sci. **253**, 6716 (2007).
[104]M. Darnon *et al.*, Microelectron. Eng. **85**, 2226 (2008).
[105]S. Vitale and H. Sawin, J. Vac. Sci. Technol., A **20**, 651 (2002).
[106]D. Eon, M. Darnon, T. Chevolleau, T. David, L. Vallier, and O. Joubert, J. Vac. Sci. Technol., B **25**, 715 (2007).
[107]V. Raballand, G. Cartry, and C. Cardinaud, J. Appl. Phys. **102**, 063306 (2007).
[108]R. Hsiao, D. Miller, and A. Kellock, J. Vac. Sci. Technol. A **14**, 1028 (1996).
[109]B. Tsui and K. Fang, IEEE Trans. Semicond. Manuf. **18**, 716 (2005).
[110]D. Zhuang and J. Edgar, Mater. Sci. Eng., R **48**, 1 (2005).
[111]K. Williams and R. Muller, J. Microelectromech. Syst. **5**, 256 (1996).
[112]K. Williams, K. Gupta, and M. Wasilik, J. Microelectromech. Syst. **12**, 761 (2003).
[113]S. Pauliac-Vaujour, P. Brianceau, C. Comboroure, and O. Faynot, J. Vac. Sci. Technol., B **31**, 021603 (2013).
[114]C. Ho, X. Lin, H. Chien, and C. Lien, Thin Solid Films **518**, 6076 (2010).
[115]L. Meng, C. Li, X. He, J. Luo, C. Zhao, and J. Yan, Microelectron. Eng. **127**, 7 (2014).
[116]H. Hody, V. Paraschiv, E. Vecchio, S. Locorotondo, G. Winroth, R. Athimulam, and W. Boullart, J. Micro-Nanolithogr. MEMS, MOEMS **12**, 041306 (2013).
[117]S. Pauliac-Vaujour, P. Brianceau, C. Comboroure, and O. Faynot, Microelectron. Eng. **85**, 800 (2008).
[118]M. Baklanov, J. de Marneffe, D. Shamiryan, A. Urbanowicz, H. Shi, T. Rakhimova, H. Huang, and P. Ho, J. Appl. Phys. **113**, 041101 (2013).
[119]F. Chen, W. Chen, M. Tsai, and T. Ku, J. Micro-Nanolithogr. MEMS, MOEMS **13**, 011008 (2014).
[120]V. Miikkulainen, M. Leskela, M. Ritala, and R. Puurunen, J. Appl. Phys. **113**, 021301 (2013).
[121]D. Li, M. Guruz, C. Bhatia, and Y. Chung, Appl. Phys. Lett. **81**, 1113 (2002).

13 November 2025 14:59:35

Micron Ex. 1032, p. 19
Micron v. YMTC
IPR2025-00117